

FABRICATION AND CHARACTERIZATION OF ZINC OXIDE LIGHT-EMITTING
DIODES, INDIUM ZINC OXIDE THIN-FILM TRANSISTORS, AND ALGAN/GAN HIGH
ELECTRON MOBILITY TRANSISTOR-BASED BIOSENSORS

By

YU-LIN WANG

A DISSERTATION PRESENTED TO THE GRADUATE SCHOOL
OF THE UNIVERSITY OF FLORIDA IN PARTIAL FULFILLMENT
OF THE REQUIREMENTS FOR THE DEGREE OF
DOCTOR OF PHILOSOPHY

UNIVERSITY OF FLORIDA

2009

© 2009 Yu-Lin Wang

To my family

ACKNOWLEDGMENTS

I would like to thank my advisor, Dr. Fan Ren, for his guidance and support. He guided me professionally and gave me personal advices. He has always shown me how to work successfully. I deeply appreciate all the opportunities he provided to me. I also thank the rest of my committee : Dr. Brent Gila, Dr. Steve Pearton, Dr. David Norton, Dr. Cammy Albernathy and Dr. Jenshan Lin.

I would like to express my special thanks to all my group members for their great assistance in many ways, Dr. Byung Sam Kang, Dr. Hung-Ta Wang, Dr. Soowan Jang, Dr. Travis Anderson, Dr. Jau-Jiun Chen, Dr. Chih-Yang Chang, Shengchun Hung, Ke-Hung Chen, Byung hwan Chu, and Chein-Fong Lo. Special thanks also go to my co-workers, Wantae Lim, Dr. Hyun-sik Kim, and Dr. Lance Covert for I had a good time working with them. I also thank Andrew Gerger and Dr. Brent Gila for their great help with our vacuum system. I thank Dr. Luc Stafford, Jonathan Wright, Dr. Lars Voss, Patric Sadik, Dr. Li-Chia Tien. Thanks also go to James Hinnant, Dennis Vince and Dr. Santiago Alves Tavares for their help in equipment maintenance. I thank Dr. Ivan Kravchenko and Bill Lewis in UF nanofab.

I particularly thank I-Lei Sun, Philip Shih, and Yo-Ho Lin for their great support. I also thank many friends from Taiwan I met here. These friends help me get through the bad times and share the good times with me.

I thank Pei-Yu Chung for giving me the chance to share our lives together. It's been one of my best times in Gainesville.

Finally, I want to thank my parents, and my family for the love they have given to me.

This dissertation can be accomplished in all because of so many people's help. I truly appreciate everyone.

TABLE OF CONTENTS

	<u>page</u>
ACKNOWLEDGMENTS.....	4
LIST OF TABLES.....	7
LIST OF FIGURES	8
ABSTRACT	10
CHAPTER	
1 INTRODUCTION.....	12
1.1 Motivation.....	12
1.1.1 ZnO Light-Emitting Diodes	12
1.1.2 Indium Zinc Oxide Thin-Film Transistors	12
1.1.3 Botulinum Neurotoxin Biosensors	13
1.1.4 <i>Perkinsus marinus</i> Biosensors	14
1.2 Study Outlines	15
2 HYDROGEN EFFECTS ON ZINC OXIDE LIGHT-EMITTING DIODES	16
2.1 Background.....	16
2.2 Hydrogen Effects on the Optical and Electrical Properties of ZnO Light-Emitting Diodes	18
2.2.1 Experimental	18
2.2.2 Results and Discussions	19
2.2.3 Summary	22
2.3 Dielectric Passivation Effects on Zinc Oxide Light-Emitting Diodes.....	26
2.3.1 Experimental	26
2.3.2 Results and Discussions	27
2.3.3 Summary	29
3 ROOM TEMPERATURE DEPOSITED DEPLETION MODE AND ENHANCEMENT MODE INDIUM ZINC OXIDE THIN FILM TRANSISTORS.....	33
3.1 Background.....	33
3.2 Depletion Mode Indium Zinc Oxide Thin-Film Transistors	37
3.2.1 Experimental	37
3.2.2 Results and Discussions	39
3.2.3 Summary	40
3.3 RF Characteristics of Small Gate Dimension of Depletion Mode Indium Zinc Oxide Thin-Film Transistors	42
3.3.1 Experimental	42
3.3.2 Results and Discussions	44

3.3.3	Summary	45
3.4	Enhancement Mode Indium Zinc Oxide Thin-Film Transistors	49
3.4.1	Experimental	49
3.4.2	Results and Discussions	50
3.4.3	Summary	51
4	ALGAN/GAN HIGH ELECTRON MOBILITY TRANSISTOR-BASED BIOSENSORS	54
4.1	Background.....	54
4.2	Botulinum Neurotoxin Biosensor.....	55
4.2.1	Experimental	55
4.2.2	Results and Discussions	57
4.2.3	Summary	57
4.3	Perkinsus Marinus Biosensors.....	61
4.3.1	Experimental	61
4.3.2	Results and Discussions	63
4.3.3	Summary	64
5	CONCLUSIONS	68
5.1	Hydrogen Effects on ZnO Light-emitting Diodes	68
5.2	Indium Zinc Oxide Thin Film Transistors.....	69
5.3	AlGaN/GaN High Electron Mobility Transistor-Based Biosensors	70
	LIST OF REFERENCES	71
	BIOGRAPHICAL SKETCH	79

LIST OF TABLES

<u>Table</u>		<u>page</u>
3-1	Comparisons of materials for TFT used in display applications.....	36
3-2	Comparisons of various conductive oxides.	37
3-3	Extracted device parasitic parameters using a T-model.	49

LIST OF FIGURES

<u>Figure</u>	<u>page</u>
2-1. Schematic of ZnO p-n light-emitting diode.	22
2-2. I-V characteristics for n-type and p-type Ohmic contacts with and without thermal annealing at 350°C under an O ₂ ambient.	23
2-3. I-V characteristics and electroluminescence intensity from a diode before and after thermal annealing at 350°C for 5 minutes under an O ₂ ambient.	23
2-4. I-V characteristics and Electroluminescence of an annealed diode before and after D ₂ plasma treatment.	24
2-5. Characteristics of an annealed diode, which was treated in air, water, and diluted phosphoric acid solution.	24
2-6. Electroluminescence spectrum of an annealed diode with and without diluted phosphoric acid treatment.	25
2-7. Graph of a ZnO based heterojunction LED.	29
2-8. I-V and light emission from a SiO ₂ passivated ZnO LED.	30
2-9. I-V and light emission from a SiN _x passivated ZnO LED.	31
2-10. FTIR spectra of the unpassivated, SiN _x passivated, and SiO ₂ passivated LED.	32
3-1. Wavefunction overlap integral of ns orbitals for various metal oxides. ⁽¹²³⁾	36
3-2. A depletion mode IZO TFT with SiO ₂ gate dielectric.	40
3-3. I _{DS} -V _{DS} characteristics at 0V gate bias from IZO transistors with 50 nm thick SiO ₂ gate dielectric.	41
3-4. I _{DS} and g _m as a function of V _{GS} for a device with 50 nm SiO ₂ gate (the inset shows the data in log-linear form).	41
3-5. I _G -V _G for devices with two different SiO ₂ gate dielectric thicknesses.	42
3-6. An depletion mode IZO TFT with SiN _x gate dielectric.	45
3-7. I _{ds} -V _{ds} characteristics of a typical depletion mode IZO TFT with gate-dimension of 1 μm × 200μm.	46
3-8. DC characteristics of a typical depletion mode IZO TFT.	47
3-9. RF characteristics of a depletion mode IZO TFT.	48

3-10. A simplified equivalent circuit of IZO TFT.....	49
3-11. Schematic of an enhancement mode IZO-TFT.....	51
3-12. I_{ds} - V_{ds} characteristics of an enhancement IZO TFT with gate-dimension of $2 \mu\text{m} \times 200\mu\text{m}$	52
3-13. Graph characteristics for enhancement mode IZO TFT measured at $V_{ds}=2V$	52
4-1. Schematic of AlGaIn/GaN HEMT sensor. The Au-coated gate area was functionalized with anti-botulinum antibody/ botulinum antigen on thioglycolic acid	58
4-2. DC response of the antibody-functionalized AlGaIn/GaN HEMT to botulinum toxin	59
4-3. Change of drain current versus different concentrations from 0.1 ng/ml to 100 ng/ml of botulinum toxin.	60
4-4. The real-time test from a used sensor which was washed with PBS in pH 5 to refresh the sensor.	60
4-5. The real-time test from a used sensor which had been fabricated for 3 months.	61
4-6. Schematic of AlGaIn/GaN HEMT sensor. The Au-coated gate area was functionalized with anti- <i>Perkinsus marinus</i> antibody/ <i>Perkinsus marinus</i> antigen on thioglycolic acid.	64
4-7. DC response of the antibody-functionalized AlGaIn/GaN HEMT to <i>Perkinsus marinus</i> -infected sea water.	65
4-8. Drain current of an AlGaIn/GaN HEMT versus time for <i>P. marinus</i> detection in the original sea water.	66
4-9. Real-time detection of <i>P. marinus</i> in an infected sea water from the tank 2.	67

Abstract of Dissertation Presented to the Graduate School
of the University of Florida in Partial Fulfillment of the
Requirements for the Degree of Doctor of Philosophy

FABRICATION AND CHARACTERIZATION OF ZINC OXIDE LIGHT-EMITTING
DIODES, INDIUM ZINC OXIDE THIN-FILM TRANSISTORS, AND ALGAN/GAN HIGH
ELECTRON MOBILITY TRANSISTOR-BASED BIOSENSORS

By

Yu-Lin Wang

May 2009

Chair: Brent P. Gila
Cochair: Fan Ren
Major: Materials Science and Engineering

Hydrogen effects on the electrical and optical properties of p-i-n ZnO light emitting diodes (LEDs) were investigated. There were no diode characteristics or light emission observed from p-i-n ZnO LEDs unless the LEDs were annealed at 350 °C after fabrication. Annealed diodes showed band-edge electroluminescence at 385nm and a broad defect band with a peak at 930nm at room temperature. The effects of hydrogen plasma, moisture, water, and phosphoric acid solution on the annealed diode characteristics were investigated and significant degradation of electrical and optical properties were observed in all cases. The plasma-enhanced chemical vapor-deposited (PECVD) SiO₂ and SiN_x passivation effects on p-i-n ZnO LEDs were also investigated.

Depletion mode and enhancement mode indium zinc oxide (IZO) thin film transistors (TFTs) were fabricated on glass substrates using rf magnetron sputtering deposition at room temperature. Plasma enhanced chemical vapor deposited SiO₂ or SiN_x was used as the gate insulator. The depletion mode TFTs had a threshold voltage of -2.5V. The drain current on-to-off ratio was $>10^5$. The maximum field effect mobility in the channel was $14.5 \text{ cm}^2 \cdot \text{V}^{-1} \cdot \text{s}^{-1}$. A unity current gain cut-off frequency, f_T , and maximum frequency of oscillation, f_{max} of 180 and

155 MHz, respectively, were obtained. The equivalent device parameters were extracted by fitting the measured s-parameters to a device equivalent circuit model to obtain the device parameters; intrinsic transconductance, inductances, drain resistance, drain-source resistance, transit time and gate-drain and gate-source capacitance. The enhancement mode TFTs showed an excellent pinch-off and the threshold voltage was 0.75V. The drain current on-to-off ratio of the e-mode TFTs was $>10^6$. The maximum field effect mobility in the channel was $39.7 \text{ cm}^2 \cdot \text{V}^{-1} \cdot \text{s}^{-1}$.

Antibody-functionalized and Au-gated AlGaIn/GaN high electron mobility transistors (HEMTs) were used to detect botulinum toxin. The antibody was anchored to the gate area through immobilized thioglycolic acid. The AlGaIn/GaN HEMT drain-source current showed a rapid response of less than 5 seconds when the target toxin in a buffer was added to the antibody-immobilized surface. The detection limit is less than 1 ng/ml of botulinum. The sensors could be recycled by washing with phosphate buffered saline (PBS) solution. When the sensors were properly stored at 4°C for several months, they still could work well with an un-degraded sensitivity. By using a similar method, the bacteria, *Perkinsus marinus* (*P. marinus*), was also detected by a AlGaIn/GaN HEMT-based sensor in sea waters.

CHAPTER 1 INTRODUCTION

1.1 Motivation

1.1.1 ZnO Light-Emitting Diodes

ZnO is attracting renewed interest for use in blue/UV light-emitting diodes (LEDs) with potential advantages over the III-nitride system due to the higher exciton binding energy, availability of high quality bulk substrates and ease of wet etching⁽¹⁻⁵⁾. After the device fabrication, ZnO LEDs degraded in DC characteristics and in electroluminescent intensity within days. For ZnO LED, it has proven difficult to obtain strong and reproducible electroluminescence due to the difficulties in producing high and stable hole concentration in the p-type ZnO layer⁽⁶⁻¹²⁾. Much efforts have been put on increasing the hole concentration in the p-type ZnO. Limited works have been done on unwanted donor impurity diffusing into the ZnO during the fabrication and storage, and the p-type characteristics of the ZnO film would disappear, leading to the degradation of the ZnO LEDs in electric and electroluminescent properties. For example, hydrogen may play a role in affecting the conductivity of ZnO films. Hydrogen is known to be a shallow donor in ZnO⁽¹³⁻³⁷⁾ and has been used to increase conductivity in n-type ZnO⁽¹⁶⁾. In this study, the effects of hydrogen passivation on ZnO LED degradation were investigated, which included how to recover the degraded ZnO LEDs and how to protect the recovered ZnO LEDs from degradation by hydrogen again.

1.1.2 Indium Zinc Oxide Thin-Film Transistors

Flexible electronics is emerging rapidly^(38,39). These devices have the advantages such as low profile, light weight, small size, and better performance. In displays, thin film transistors (TFTs) are used as switching components in the active-matrix over a large area. Currently, liquid crystal displays (LCDs) mostly use amorphous Si as the channel in TFTs. However, due to low

mobility ($<1 \text{ cm}^2/\text{Vs}$)⁽⁴⁰⁾ and high process temperature (350°C)⁽⁴⁰⁾, amorphous Si-TFTs are not available for high resolution displays fabricated on cheap plastic substrates. Organic TFTs also have a very low mobility ($< 1 \text{ cm}^2/\text{Vs}$)⁽⁴⁰⁾ and may have reliability concerns⁽⁴⁰⁾. Oxide-based TFTs have mobility ($10\sim 50 \text{ cm}^2/\text{Vs}$) that is at least 1 order higher^(41,42) than that of amorphous Si-TFTs and organic TFTs and can be deposited at room temperature. Because of the high electron mobility, oxide-based TFTs are not only available for switching active arrays for high resolution displays but also can replace driver-integrated circuits (driver ICs) that usually use crystalline silicon transistors. The integration of active arrays and driver ICs can reduce cost and provide a more compact display. In addition, oxide-based TFTs have other advantages such as room temperature deposition, higher transparency, better smoothness, etc.^(43~45). Thus, the oxide-based TFT based technology has a great potential to be used to realize the roll-to-roll type display. If this technology can be realized, it can not only replace the current amorphous Si-TFTs for LCDs, but also create new applications on various sets such as heads-up, windshield, electronic books or light weight computers thus changing the whole display industry.

1.1.3 Botulinum Neurotoxin Biosensors

Biological weapons are particularly attractive tools for terror because biological agents are available and easy to manufacture. Only small amounts of toxins are required to cause large-scale effects, and such attacks can easily overwhelm existing medical resources. Reliable and fast detection of biological agents in the field and in real time has proved to be challenging. Clostridium botulinum neurotoxins are among the most deadly toxins and are listed as a NIAID—Category A agent for bioterrorism potential. The lethal dose in unvaccinated humans is estimated at 1 ng/kg ^(46,47). Conventional methods of detection involve the use of HPLC, mass spectrometry and colorimetric ELISAs; but these are impractical because such tests can only be

carried out at centralized locations, and are too slow to be used as the real time detection in the field⁽⁴⁸⁻⁶⁰⁾. Another test for botulinum toxin detection is the ‘mouse assay’, which relies on the death of mice as an indicator of toxin presence⁽⁶¹⁾. Clearly, such methods are slow and impractical in the field. In order to create a botulinum sensor with a fast response and low detection limit in field, the AlGaIn/GaN high electron mobility transistors (HEMTs) were used. AlGaIn/GaN HEMTs were successfully used for several medical sensing applications⁽⁶²⁻⁷⁵⁾. This is due to a high electron sheet carrier concentration channel induced by both piezoelectric polarization and spontaneous polarization. Unlike conventional semiconductor field effect transistors, there is no intentional dopant in the AlGaIn/GaN HEMT structure. The electrons in the two-dimensional electron gas (2DEG) channel are located at the interface between the AlGaIn layer and GaN layer and there are positive counter charges at the HEMT surface layer induced by the 2DEG. Slight changes in the ambient can affect the surface charge of the HEMT, thus changing the 2DEG concentration in the channel. Once the gate area of the HEMT sensors is immobilized with anti-botulinum antibodies, the sensors can be used to detect the botulinum toxin specifically with high sensitivity.

1.1.4 *Perkinsus marinus* Biosensors

Perkinsus species (*Perkinsozoa*, *Alveolata*) are the causative agent of perkinsosis in a variety of mollusc species. *Perkinsus* species infections cause widespread mortality in both natural and farmed oyster populations, resulting in severe economic loss for the shellfishery, and detrimental effects on the environment⁽⁷⁶⁻⁸⁰⁾. Currently, the standard diagnostic method for *Perkinsus* species infections has been the fluid thioglycollate medium (FTM) assay detection⁽⁸¹⁾. However, it takes several days to do the detection. Polymerase chain reaction (PCR)-based technique is also used to determine the *Perkinsus* species but it is more expensive, time-consuming, and requires exquisite controls to assure specificity and accuracy⁽⁸²⁾. Clearly, such

methods are slow and impractical in the field. Therefore, it is important to develop a fast, cheap, and easy-to-used biosensors to detect *P. marinus*. AlGaN/GaN HEMTs are very suitable for this bio-detection because it can fit all these requirements.

1.2 Study Outlines

In this dissertation there are three research topics presented. Chapter 1 introduces the motivations of these three topics: ZnO LEDs, Indium Zinc Oxide thin-film transistors, and AlGaN/GaN HEMT-based biosensors. Chapter 2 talks about the hydrogen effects on the optical and electrical properties of ZnO LEDs. It discusses why hydrogen can diffuse into ZnO films and act as shallow donors to degrade the ZnO LEDs and how we can eliminate the hydrogen effects and protect the ZnO LEDs. Chapter 3 discusses the fabrication and characterization of the depletion mode and enhancement mode indium zinc oxide thin-film transistors. DC and RF performance were measured to demonstrate the superior performance of these TFTs. Chapter 4 presents the AlGaN/GaN HEMT-based botulinum neurotoxin biosensor and the *Perkinsus marinus* bacteria biosensor. It shows the response time, detection limit, reproducibility, recyclability and reliability. Chapter 5 gives a conclusion about this dissertation.

CHAPTER 2
HYDROGEN EFFECTS ON ZINC OXIDE LIGHT-EMITTING DIODES

2.1 Background

ZnO is attracting renewed interest for use in blue/UV light-emitting diodes (LEDs) with potential advantages over the III-nitride system due to the higher exciton binding energy, availability of high quality bulk substrates and ease of wet etching⁽¹⁻⁵⁾. However, it has proven difficult to obtain strong and reproducible electroluminescence due to the difficulties in producing high and stable hole concentration in the p-type ZnO layer.⁽⁶⁻¹²⁾ Much attention has been paid on how to activate the acceptor dopants in p-type ZnO and it is becoming clearer that the unwanted donor impurities, such as hydrogen, may play a role in influencing the conductivity of the p-type ZnO⁽¹³⁻³⁷⁾.

Hydrogen is known to be a shallow donor in ZnO⁽¹³⁻³⁷⁾ and has been used to increase conductivity in n-type ZnO⁽¹⁶⁾. Two donor activation energy are found, namely ED1 = 35meV and ED2= 66meV⁽²⁰⁾. When considering the thermal energy 25.7meV at room temperature (298K), it is obvious that the donor activation of hydrogen is quite low making the hydrogen a shallow donor in a ZnO film. It is predicted that interstitial hydrogen (²H or ¹H) atoms introduce shallow states in ZnO films⁽¹⁴⁾. Experimental data of its nuonium counterpart from electron paramagnetic resonance has proved it⁽⁸³⁾.

Hydrogen can be easily incorporated into ZnO during epi-layer growth and device fabrication. Diffusivity and the diffusion activation energy were extracted from experiments incorporating hydrogen (or deuterium) plasma, ion implantation or nuonium counterpart into bulk ZnO film⁽²²⁾. The activation energy for deuterium and hydrogen are 0.17eV+/-0.12eV and 60meV, respectively, which are not very high compared to 1kT (25.7meV) at room temperature (298K)⁽²²⁾. It was also reported that the applied external electrical current or field can induce the

hydrogen migration in ZnO^(84, 85). Since high p-type doping levels in ZnO are difficult to achieve, hydrogen may easily compensate the hole concentration in the p-type ZnO and convert it to n-type. Although hydrogen atoms can easily diffuse into ZnO films, they also can be driven out of the films by thermal annealing at 300-900 °C, as verified by experiments using secondary ion mass spectroscopy (SIMS)^(22, 23, 84~87). If the p-type ZnO is compensated by hydrogen incorporation, a simple thermal annealing may reverse the process of hydrogen incorporation through the high diffusivity and the considerably low diffusion activation energy of hydrogen. With this approach, a hydrogen-degraded ZnO LED could be recovered.

Plasma-enhanced chemical vapor-deposited (PECVD) SiN_x and SiO₂ have been widely used for passivating GaAs and InP LEDs and lasers⁽⁸⁸⁾. These dielectrics have also been used to passivate n-type Li- and Cu- doped ZnO to preserve the surface conductivity⁽⁸⁹⁾. SiN_x capped ZnO showed a surface channel existing either under vacuum or air ambient. SiO₂ capped ZnO showed similar results but became unstable at high temperature⁽⁸⁹⁾.

In this work, the effect of hydrogen on the electrical and optical properties of ZnO LEDs is investigated. Hydrogen was intentionally introduced into the LEDs through hydrogen plasma treatments, exposure to air, dipping the samples into DI water or diluted H₃PO₄ solutions. The current-voltage (I-V), light intensity and electroluminescence (EL) of the diodes were measured to characterize the effect of the hydrogen treatments. Moreover, we have also investigated the passivation effects of PECVD SiO₂ and SiN_x on ZnO-based heterojunction p-i-n LEDs. The diode current-voltage (I-V), electroluminescence (EL), and intensity-current (L-I) of the diodes were measured to characterize the passivation effects on ZnO LEDs. Fourier transfer infrared (FTIR) spectroscopy was used to identify hydrogen incorporation in the dielectric film during the dielectric depositions and after post deposition annealing.

2.2 Hydrogen Effects on the Optical and Electrical Properties of ZnO Light-Emitting Diodes

2.2.1 Experimental

The LED structure consisted of 250 nm of P doped ZnO, 40 nm of i-Zn_{0.9}Mg_{0.1}O, 40 nm of i-ZnO, 40 nm of i-Zn_{0.9}Mg_{0.1}O, and 450 nm of Ga doped ZnO. The epitaxial films were grown on c-plane sapphire substrates by pulsed laser deposition (PLD) at a substrate temperature of 700 °C. Ga and P were used as the n- and p-type dopants, respectively. Prior to LED epitaxial film deposition, an undoped ZnO buffer layer was deposited on the sapphire at 400°C and a pressure of 20 mTorr as a nucleation layer. This buffer layer was annealed at 650 °C. The LED epitaxial films were grown in an oxygen partial pressure of 150 mTorr. Phosphorus-doped ZnO targets were fabricated using high purity (99.99955 %) ZnO mixed with P₂O₅(99.998 %) as the doping agent and the phosphorus doping levels was 0.5 at. %. Gallium-doped ZnO targets were fabricated with high purity (99.99955 %) ZnO mixed with Ga(99.998 %) as the doping agent and the gallium doping level was 1 at. %. The carrier concentration in the P and Ga doped ZnO layers were approximately $1 \times 10^{17} \text{ cm}^{-3}$ and $5 \times 10^{19} \text{ cm}^{-3}$, respectively, based on single layer Hall measurements. All targets were sintered at 1000°C for 12 hours in air. The targets were ablated with a KrF excimer laser with the laser frequency of 1 Hz and energy density of approximately 1.5 J/cm².

Prior to the LED fabrication, the ZnO multilayered structures were annealed in a rapid thermal annealing (RTA) system at 850 °C for 1 min under an oxygen ambient to activate p-type dopant⁽⁸⁸⁾. The carrier concentration and the mobility of holes were $1 \times 10^{17} \text{ cm}^{-3}$ and $1 \text{ cm}^2/\text{V}\cdot\text{sec}$, respectively. The LED fabrication started with device isolation and followed by p-mesa definition using dilute phosphoric acid solution. Electron beam deposited Ni (20nm)/Au (80nm) and Ti (20nm)/Au(80nm) were used as the p- and n-Ohmic metallization. A schematic of the

LED diode is shown in Figure 2-1. The diode current-voltage (I-V) characteristics were measured at 300K using a probe station and Agilent 4145B parameter analyzer. The electroluminescence (EL) spectra and output power were measured using a spectrometer and Si photodiode, respectively.

2.2.2 Results and Discussions

As mentioned in the previous paragraph, the p-ZnO epitaxial films converted to p-type conductivity after the post-growth RTA procedure at 850 °C, which was confirmed with Hall measurements. However, after the LED diodes were fabricated, the top p-ZnO layer became much more conductive, as seen in Figure 2-2 which shows the I-V characteristics measured from a transmission line pattern across a gap of 16 μm. The conductivity of the n-ZnO was consistent with the $5.1 \times 10^{19} \text{ cm}^{-3}$ doping level in the n-layer. However, the conductivity of p-ZnO was much higher than the intentional doping of $1.1 \times 10^{17} \text{ cm}^{-3}$. The conductivity of the p-ZnO decreased significantly after annealing at 350 °C under an O₂ ambient for 90 seconds and further reduced to the range of a typical p-ZnO single epitaxial film for another 5 minutes annealing at 350 °C. There was only a slight decrease of the conductivity for the bottom n-ZnO layer after 5 min annealing.

The diode I-V characteristics and the EL intensity of the diode also showed significant differences before and after annealing at 350 °C for 5 minutes under an O₂ ambient, as shown in Figure 2-3. For the as-fabricated diode, the I-V curve was linear. There was no diode rectifying characteristic observed and no light emission either. It appeared that there was no p-n junction existing in the diode structure as the I-V showed Ohmic-like characteristics. After the diode was annealed at 350 °C for 5 mins, electroluminescence emission was detected and the diode I-V also showed rectifying characteristics. Apparently, the surface and mesa sidewalls of the top P-

doped ZnO layer of the LED was converted to n-type during the diode fabrication and the 350 °C annealing restored the p-type of the P-doped ZnO layer.

The phosphorus dopant has been suggested to have an amphoteric doping behavior in ZnO. All as-grown samples have n-type conductivity,⁽⁷⁾ and a high temperature (850 °C) post annealing causes a carrier type conversion for the P-doped ZnO film into p-type material^(88,90). However, the 350 °C annealing used in our experiment to restore the diode characteristics was too low to cause activation of the P acceptor state as suggested for the high temperature annealing conditions. One of the possibilities of the cause of p-type ZnO converting to n-type during the fabrication and restoring with low temperature annealing was hydrogen incorporation at or near the surface. Hydrogen was reported as a shallow donor in ZnO and the unintentional doping level of the hydrogen was around $6 \times 10^{16} \text{ cm}^{-3}$ ⁽²⁰⁾. The hydrogen can be easily incorporated into the ZnO epi-layers during the diode fabrication. The n-type doping level of the Ga-doped layer in the LED was $5.1 \times 10^{19} \text{ cm}^{-3}$. The conductivity of this n-ZnO would not be affected by moderate hydrogen incorporation or the 350 °C annealing, as shown in Figure 2-2. The p-type doping of the LED was $1 \times 10^{17} \text{ cm}^{-3}$, which could be easily compensated by the hydrogen either in the bulk or in the near-surface region of the film. Thus the 350 °C anneal would have significant impact on the diode characteristics through compensation of the acceptors in the p-ZnO.

In order to confirm the effects of hydrogen on the LED, a deuterium plasma was performed to treat on the LED samples. The plasma treatment was conducted in a Plasma Therm 790 plasma enhanced chemical vapor deposition system with 30W of rf (13.56 MHz) power at a pressure of 900 mTorr. The substrate temperature was held at 100 °C for 75 minutes. The diode I-V characteristics and light emission before and after the plasma treatment are shown in Figure

2-4. Although the diode characteristics did not become fully Ohmic, they displayed significantly higher leakage currents under reverse bias. The diode turn-on voltage was less than 0.3V and the diode EL intensity almost disappeared completely. The increase of leakage current in the reverse bias and the reduction of turn-on voltage indicated that the p-type carrier concentration had been compensated by the deuterium.

Hydrogen may also be introduced from other common process steps, such as wet chemical etching or simple DI water rinse. Figure 2-5 A) shows the I-V characteristics for the diodes exposed to air for 96 hours after fabrication, dipped in DI water for 3.5 hours or exposed to H₃PO₄ solution (H₃PO₄ : H₂O = 1 : 4000) for 30 sec. The diode characteristics in the forward bias region only changed slightly. However, the reverse leakage current increased noticeably after the treatments, which was also reflected in the diode EL intensity, as shown in Figure 2-5 B). There was 10-15% reduction of the EL for the diode exposed to air for 96 hours, 60% reduction for the diode dipped in DI water for 3.5 hours and 80% reduction for the diode exposed to the H₃PO₄ solution for 30 sec. With an annealing at 350 °C for 5 min, the diode EL intensity and I-V at reverse bias recovered for all the treated diodes. This indicates that the hydrogen compensation effect is recoverable and that it is important to identify how to passivate the ZnO diode from degradation.

Figure 2-6 shows the EL spectrum measured in the range from 350nm to 1050nm at 263 K for the annealed device and the device given the H₃PO₄ solution treatment. For the annealed device, a peak at 385nm resulting from band-edge emission was observed. There was another broad band peak ranging from around 500nm to 1000nm with the highest intensity at 930nm, which is usually ascribed to point defects in ZnO⁽⁸⁹⁾. It has been reported that metal/ZnO Schottky diodes exhibit the infra-red (IR) emission from defects, impurity centers or the

transition of hot carrier between states in the conduction band⁽⁸⁹⁾. The band-edge emission of the H₃PO₄ solution treated sample disappeared. It is very important to eliminate hydrogen compensation effect to achieve band-edge emission in injection LEDs in the ZnO system.

2.2.3 Summary

In conclusion, hydrogen is a shallow donor which can degrade ZnO p-n diodes in terms of both electrical and optical performance. Deuterium plasma exposure was used to verify the hydrogen compensation effect on ZnO p-n diode characteristics. Moisture, water, and H₃PO₄ solution can also introduce the hydrogen and degrade diodes. Eliminating the hydrogen compensation effect is necessary to achieve band-edge emission. Non-hydrogen containing passivation layers will be needed for the ZnO based p-n diode.

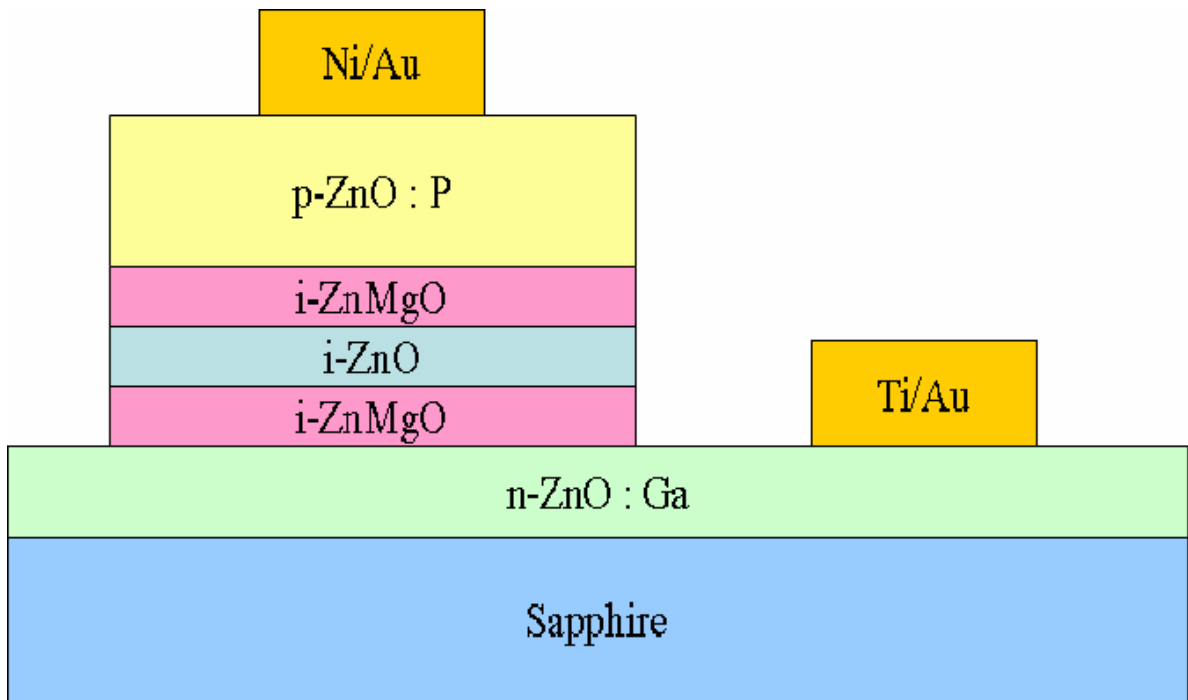


Figure 2-1. Schematic of ZnO p-n light-emitting diode.

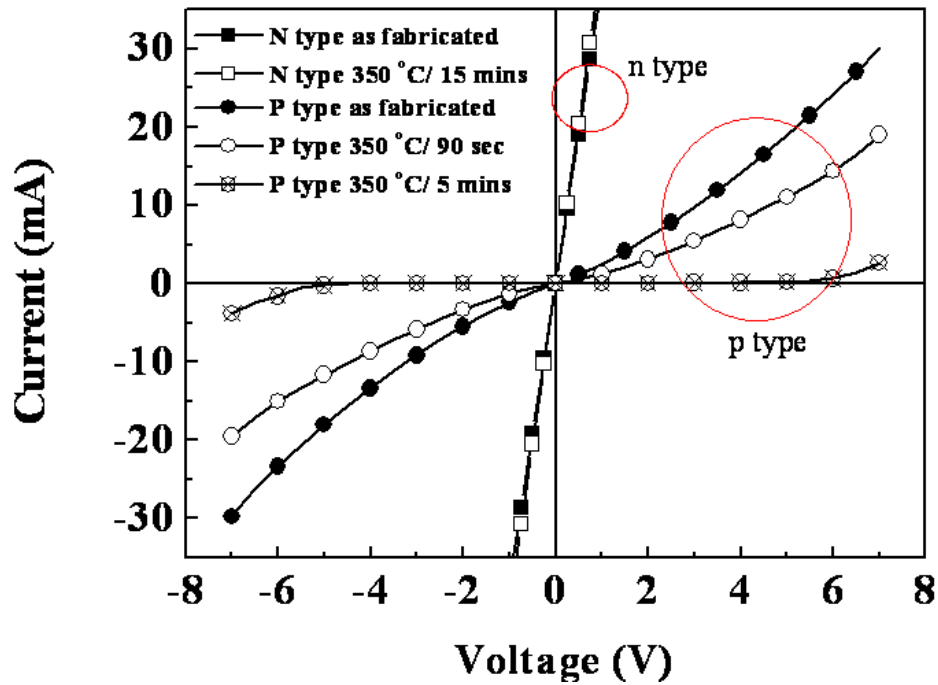


Figure 2-2. I-V characteristics for n-type and p-type Ohmic contacts with and without thermal annealing at 350°C under an O₂ ambient.

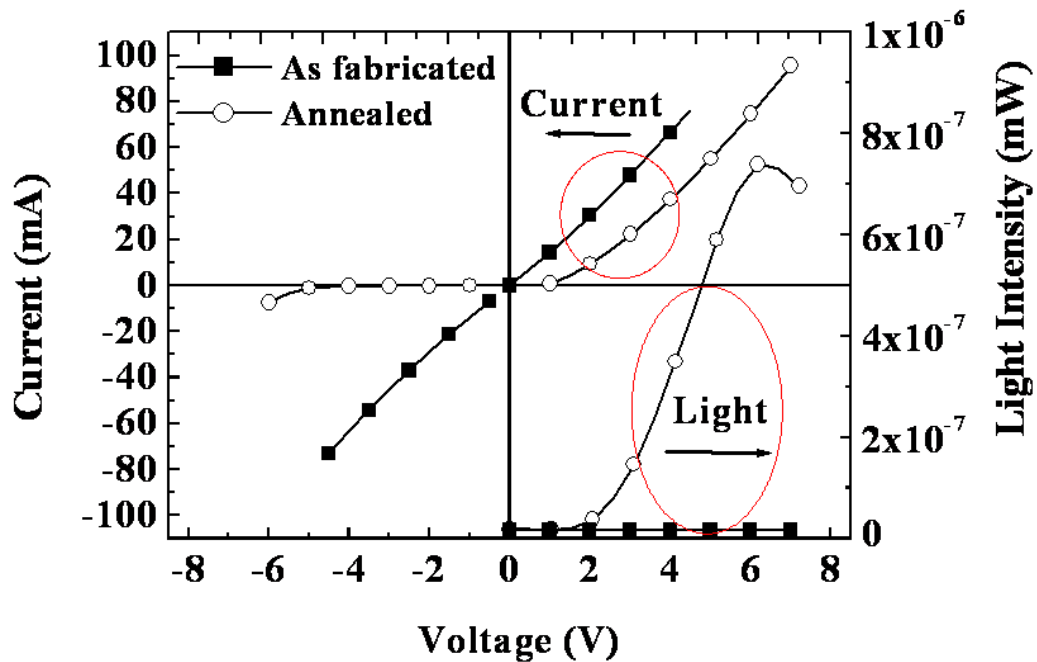


Figure 2-3. I-V characteristics and electroluminescence intensity from a diode before and after thermal annealing at 350°C for 5 minutes under an O₂ ambient.

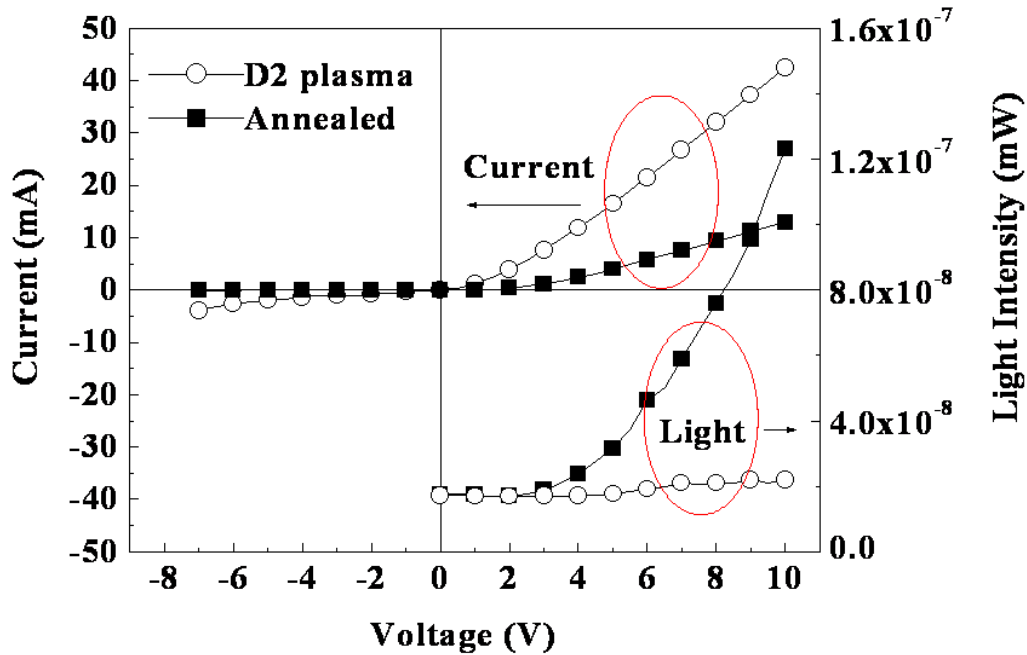
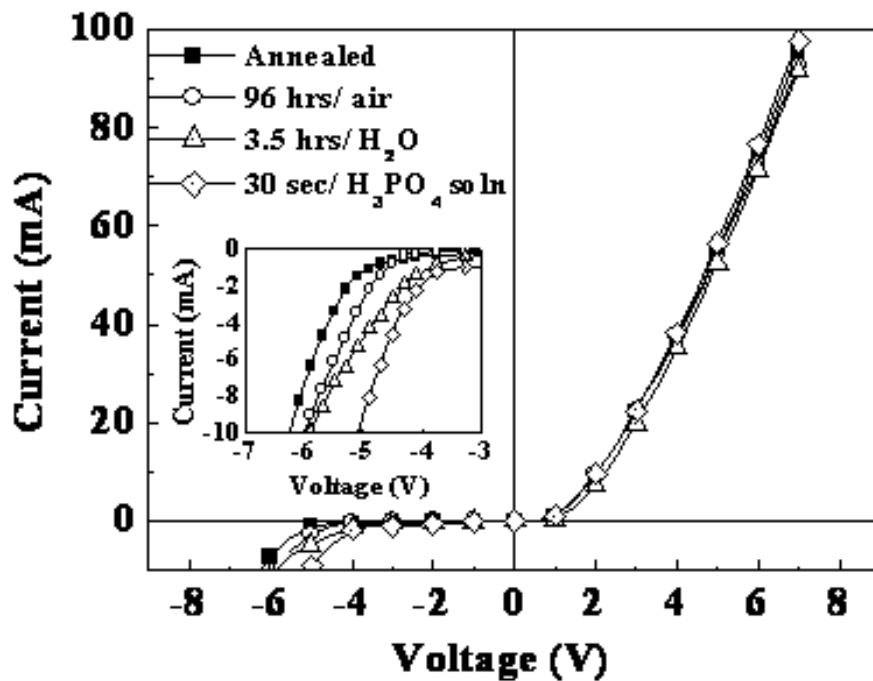
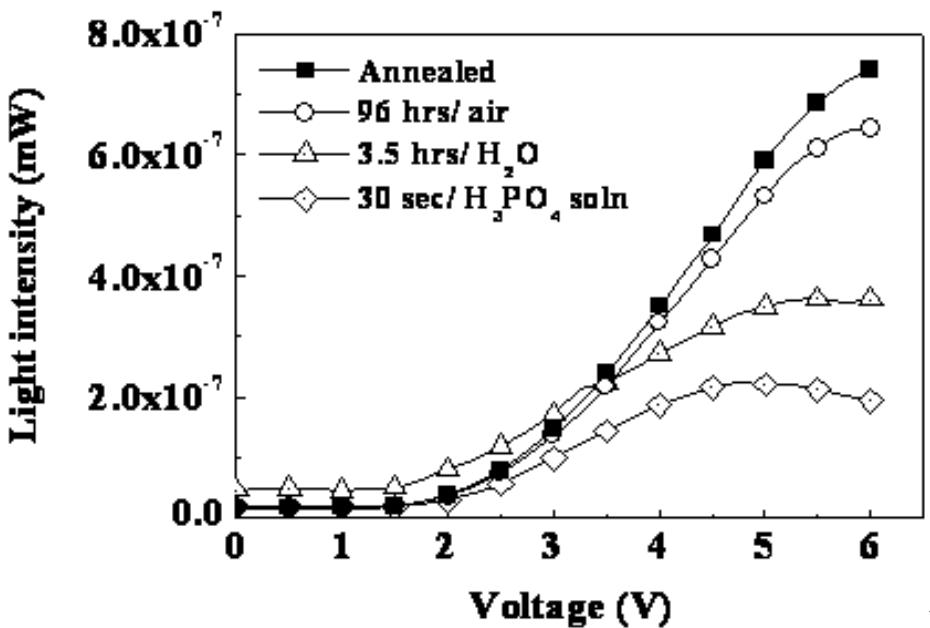


Figure 2-4. I-V characteristics and Electroluminescence of an annealed diode before and after D₂ plasma treatment.



A)

Figure 2-5. Characteristics of an annealed diode, which was treated in air, water, and diluted phosphoric acid solution. A) I-V characteristics and B) Electroluminescence intensity



B)

Figure 2-5. Continued

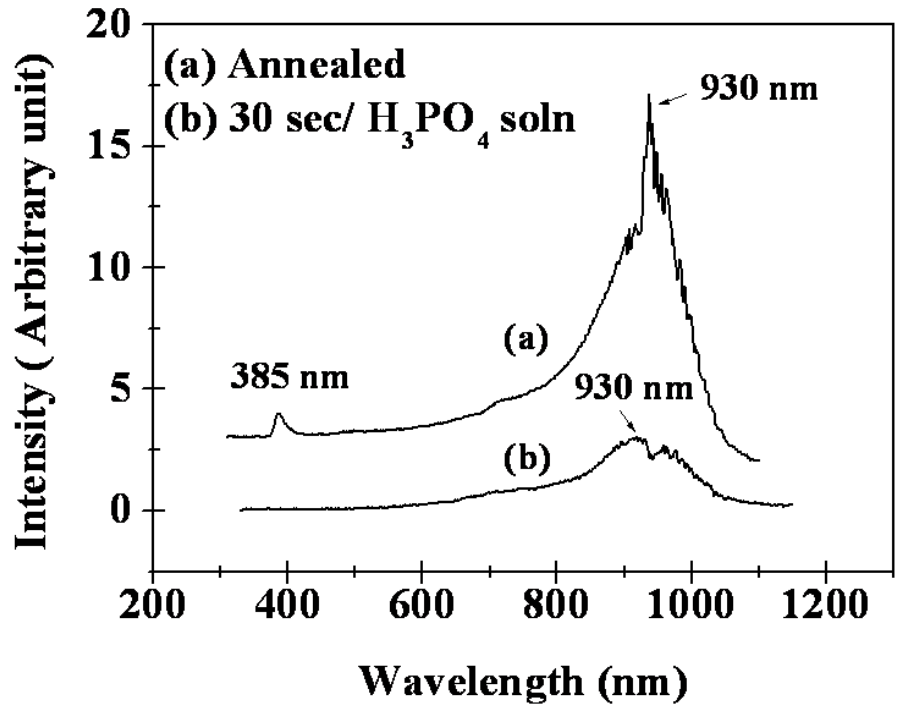


Figure 2-6. Electroluminescence spectrum of an annealed diode with and without diluted phosphoric acid treatment.

2.3 Dielectric Passivation Effects on Zinc Oxide Light-Emitting Diodes

2.3.1 Experimental

The dielectric passivation effects on ZnO LEDs were studied through PECVD SiO₂ and SiN_x. The LED structure consisted of 250 nm of phosphorus (P) doped ZnO, 40 nm of Zn_{0.9}Mg_{0.1}O, 40 nm of i-ZnO, 40 nm of Zn_{0.9}Mg_{0.1}O, and 450 nm of gallium (Ga) doped ZnO. The epitaxial films were grown on c-plane sapphire substrates by pulsed laser deposition at a substrate temperature of 700 °C. Ga and P were used as the n- and p-type dopants, respectively. Prior to LED epitaxial film deposition, an undoped ZnO buffer layer was deposited on the sapphire at 400°C as a nucleation layer. This layer was annealed at 650 °C. The epitaxial films were grown in an oxygen partial pressure of 150 mTorr. P-doped ZnO targets were fabricated using high purity (99.99955 %) ZnO mixed with P₂O₅ (99.998 %) as the doping agent and the P doping level was 0.5 at.%. Ga-doped ZnO targets were fabricated with high purity (99.99955 %) ZnO mixed with Ga(99.998 %) as the doping agent and the Ga doping level was 1 at.%. The carrier concentration in the P and Ga doped ZnO layers were $1 \times 10^{17} \text{ cm}^{-3}$ and $5 \times 10^{19} \text{ cm}^{-3}$, respectively, based on single layer Hall measurements. The targets were ablated with a KrF excimer laser with frequency of 1 Hz and energy density of approximately 1.5 J/cm^2 .

Prior to the LED fabrication, the ZnO structures were annealed in a rapid thermal annealing (RTA) system at 850 °C for 1 min under oxygen ambient to activate the p-type dopants⁽⁹⁰⁾. The carrier concentration and the mobility of holes were $\sim 10^{17} \text{ cm}^{-3}$ and $1 \text{ cm}^2/\text{V}\cdot\text{sec}$, respectively. The LED fabrication started with device isolation and followed by p-mesa definition using dilute phosphoric acid solution. The PECVD-SiO₂ and SiN_x of 300 nm were then deposited at 260 °C after mesa formation. Photoresist was used as the mask for ohmic metal contact window opening on SiO₂ or SiN_x. Electron beam deposited Ni (20nm)/Au (80nm) and Ti (20nm)/Au(80nm) were used as the p- and n-Ohmic metallization, respectively. Figure 2-

7 shows a schematic of the LED A) and optical microscope plan view B). The diode I-V characteristics were measured at 300K using a probe station and Agilent 4145B parameter analyzer. The electro-luminescence (EL) and L-I curves were measured with a Si photodiode. The EL spectrum was measured with a Princeton Instrument CCD. FTIR spectroscopy was also used to identify the hydrogen incorporation in the dielectric film.

2.3.2 Results and Discussions

The phosphorus dopant has been suggested to have an amphoteric doping behavior in ZnO. All as-grown samples have n-type conductivity and a high temperature (850 °C) post annealing causes carrier type conversion for the P-doped ZnO film into p-type material⁽⁷⁾. However, after the LEDs had been fabricated, there were no diode characteristics or light emission observed. It has been reported that annealing at 350 °C under an O₂ ambient restores the diode characteristics and light emission⁽⁹³⁾. Nevertheless, the 350 °C annealing used to restore the diode characteristics was too low to cause activation of the P acceptor state as suggested for the high temperature annealing conditions. One of the possibilities of the cause of p-type ZnO converting to n-type during the fabrication and restoring with low temperature annealing was hydrogen incorporation at or near the surface of the ZnO. The n-type doping level of the Ga-doped layer was $5.1 \times 10^{19} \text{ cm}^{-3}$ and hydrogen had less impact on the n-type conductivity. The p-type doping in the LED was 10^{17} cm^{-3} , which could be easily compensated by the hydrogen either in the bulk or in the near-surface region of the film. Although hydrogen atoms can easily diffuse into ZnO films, they also can be driven out of the films by thermal annealing at 300-900 °C⁽²²⁻²⁴⁾. Thus the 350 °C anneal would have significant impact on the diode characteristics through compensation of the acceptors in the p-ZnO.

Figure 2-8 A) shows the I-V characteristics and an insert of L-I curves of PECVD SiO₂ passivated LED before and after annealing at 350 °C for 5 minutes under an O₂ ambient. There

were no diode rectifying characteristics and no light emission for the as-fabricated LEDs. The diode characteristics and the EL intensity appear after the 350 °C annealing. Figure 2-8 B) shows the EL spectrum at 263 K for the annealed SiO₂ passivated LED. A peak at 385nm resulting from band-edge emission was observed and there was another broad band peak ranging from around 500nm to 1000nm with the highest intensity at 930nm, which is usually ascribed to point defects in ZnO.

The annealed PECVD SiN_x passivated LED exhibited very different I-V and L-I characteristics as shown in Figure 2-9 A). There was no light emission observed either before or after the thermal annealing and the LED showed very leaky diode characteristics after annealing. We used CF₄ plasma to remove the SiN_x passivation layer and there was still no light emission. Instead, the diode leakage current increased as shown in Figure 2-9 B). After annealing at 350 °C for 5 minutes under O₂ ambient, the diode characteristics and the EL intensity appeared. The precursors for the deposition of SiN_x (SiH₄, N₂, and NH₃) and SiO₂ (SiH₄ and N₂O) dielectric films provide plenty of hydrogen to diffuse into ZnO and compensate the p-dopants. It is not surprising that no diode characteristics or light emission was observed for as-fabricated LEDs. For the annealed LEDs, the difference of IV characteristics and LI curves between SiO₂ and SiN_x passivated LEDs may result from residual hydrogen in the dielectric. To confirm this, we measured the FTIR spectra for unpassivated, SiO₂ passivated, and SiN_x passivated LEDs. All these samples were annealed at 350 °C for 5 minutes under an O₂ ambient before the FTIR measurements. Figure 2-10 shows that the SiN_x passivated LED has a significant concentration of hydrogen left, with absorption peaks at N-H (~3358cm⁻¹) and Si-H (~2183cm⁻¹) bonds, whereas no hydrogen bonding signals were detected either for unpassivated or SiO₂ passivated LEDs. The detected H₂O and CO₂ peaks are commonly observed as surface contamination.

These results explain why the unpassivated and SiO_2 passivated LEDs showed diode rectifying characteristics and light emission after the thermal annealing whereas not for the SiN_x -passivated LEDs.

2.3.3 Summary

In conclusion, due to the high residual hydrogen concentration in SiN_x films, post-LED-fabrication thermal annealing could not activate the diodes unless the SiN_x was removed. SiO_2 has lower residual hydrogen and a simple post-diode-fabrication anneal was enough to activate the diode characteristics.

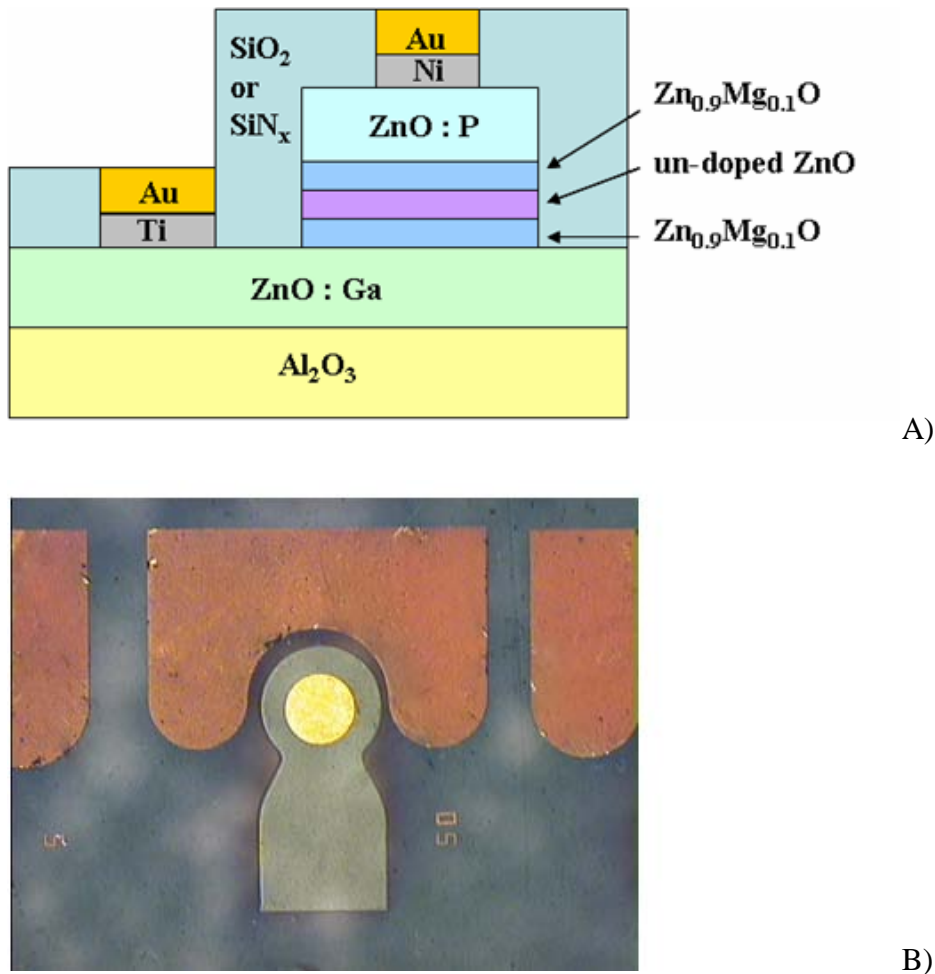
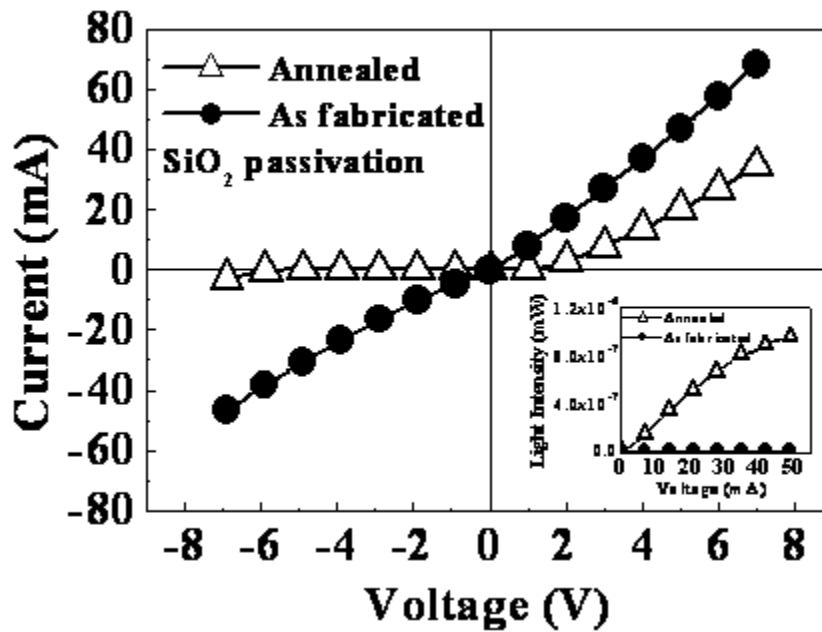
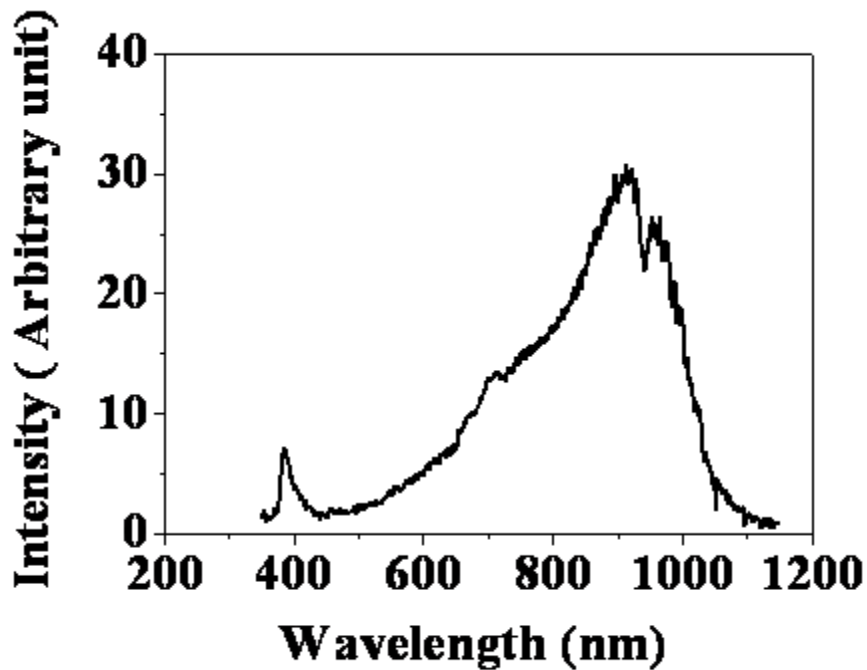


Figure 2-7. Graph of a ZnO based heterojunction LED. A) Schematic of the LED. B) Optical microscope plan view of the LED.

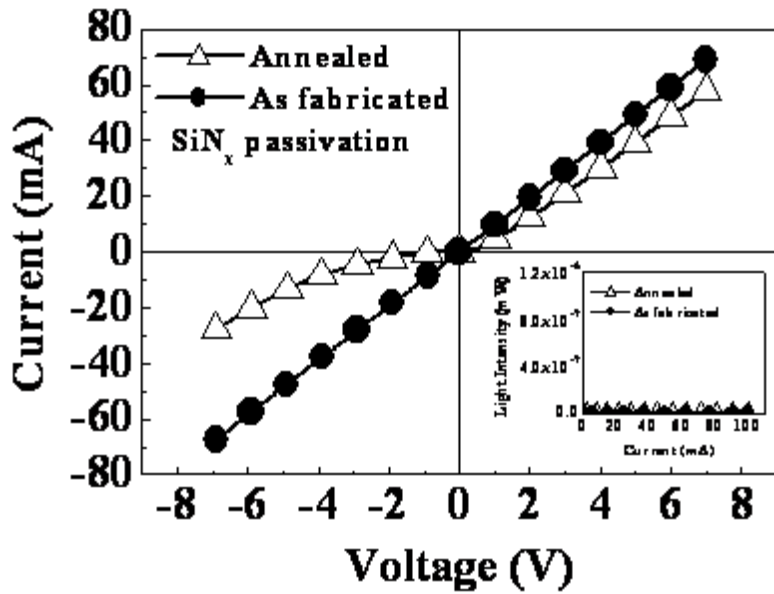


A)

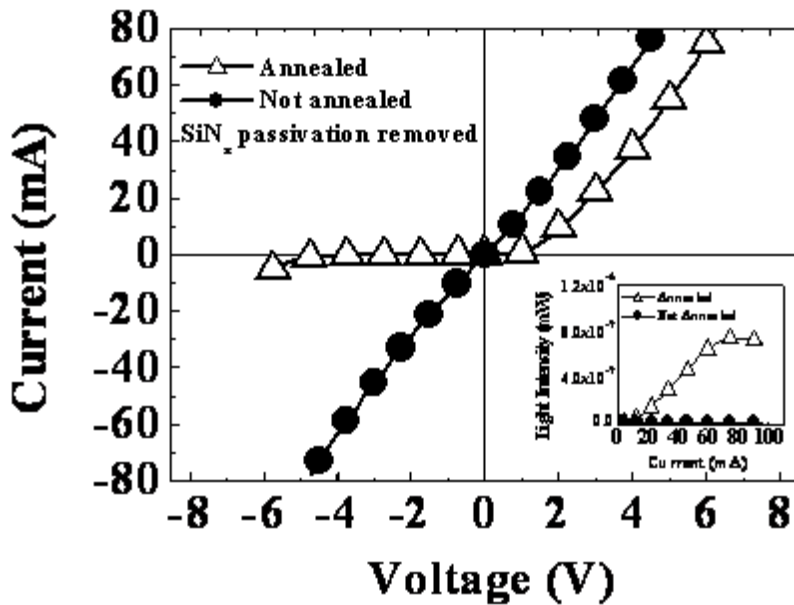


B)

Figure 2-8. I-V and light emission from a SiO₂ passivated ZnO LED. A) I-V characteristics and L-I curves of the SiO₂ passivated LED before and after thermal annealing at 350°C for 5 minutes under an O₂ ambient. B) EL spectrum of the annealed SiO₂ passivated LED.



A)



B)

Figure 2-9. I-V and light emission from a SiN_x passivated ZnO LED. A) I-V characteristics and L-I curves of a SiN_x passivated LED before and after thermal annealing at 350°C for 5 minutes under an O_2 ambient. B) I-V characteristics and L-I curves of a SiN_x passivated LED after SiN_x removal before and after thermal annealing at 350°C for 5 minutes under an O_2 ambient.

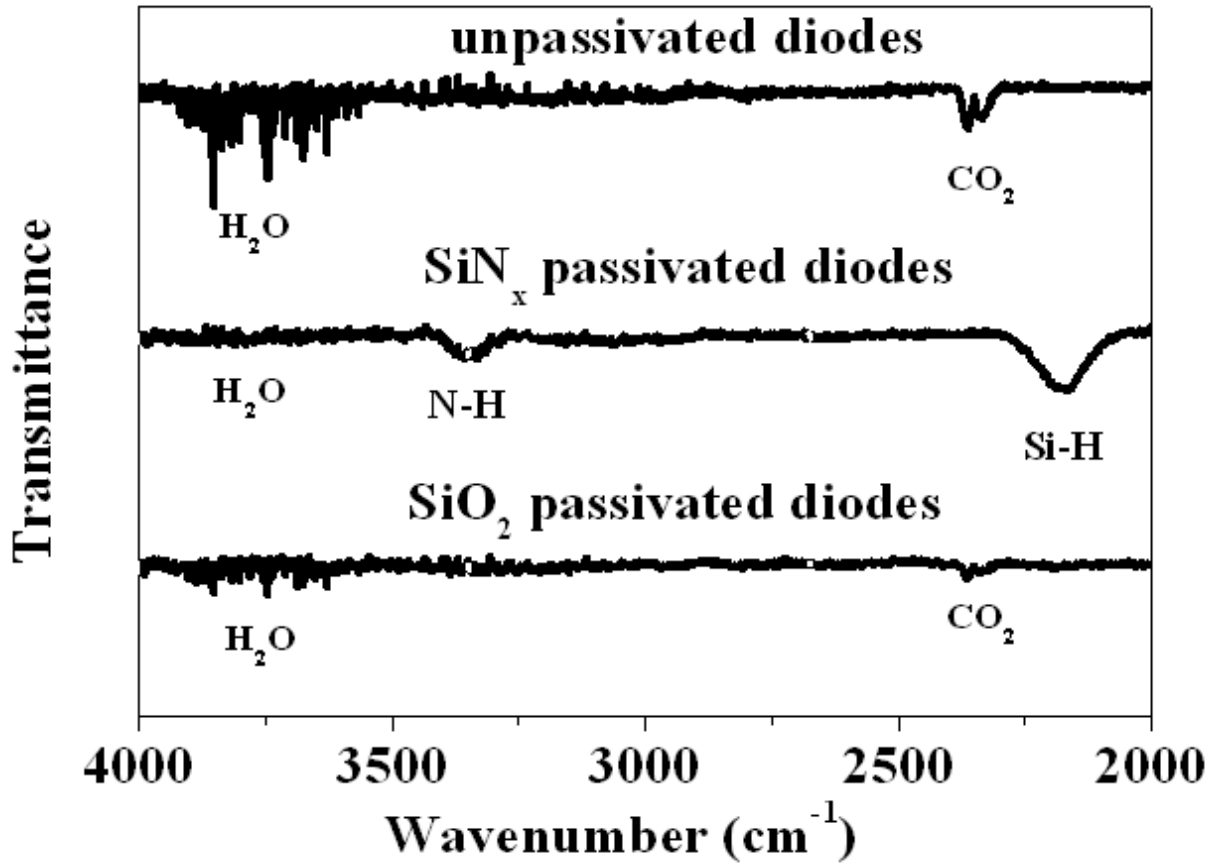


Figure 2-10. FTIR spectra of the unpassivated, SiN_x passivated, and SiO_2 passivated LED.

CHAPTER 3
ROOM TEMPERATURE DEPOSITED DEPLETION MODE AND ENHANCEMENT MODE
INDIUM ZINC OXIDE THIN FILM TRANSISTORS

3.1 Background

Transparent conductive oxides (TCOs) were applied in many areas, such as the transparent electrodes used in liquid crystal displays, solar cells, and light emitting diodes because of their high electrical conductivity and high optical transparency⁽⁹⁴⁻⁹⁶⁾. Oxide-based thin film transistors attract much attention due to their advantages such as high mobility, high electrical conductivity, and high visible transmittance⁽⁹⁷⁻¹⁰⁰⁾. Amorphous or nano-crystalline n-type oxide semiconductors such as zinc oxide, zinc tin oxide, indium gallium oxide, and indium gallium zinc tin oxide demonstrate surprisingly high carrier mobilities ($\sim 10 \text{ cm}^2/\text{Vs}$) even for amorphous films deposited at room temperature⁽¹⁰⁰⁻¹¹⁷⁾. Many transparent thin film transistors (TTFTs) were reported using crystalline ZnO^(118,119), or polycrystalline SnO₂⁽¹²⁰⁾, and In₂O₃⁽¹²¹⁾. However, to realize the transparent thin film transistor for flexible electronics, amorphous films are more suitable than crystalline type, because amorphous type oxide films have extra advantages such as low temperature deposition, good film smoothness, low compressive stress, and large area deposition by sputtering⁽⁴³⁻⁴⁵⁾. An amorphous conductive oxide, InZnO (IZO), with a high carrier mobility ($10\sim 50 \text{ cm}^2/\text{Vs}$)^(41,42), was proved a promising TCO due to its good electrical properties and thermal stability.

An amorphous or polycrystalline Si:H layer as the channel have been commonly used for most conventional TFTs in display applications. The standard Si-based TFTs have drawbacks such as light sensitivity, light-induced degradation and low field effect mobility ($< 1 \text{ cm}^2/\text{Vs}$)⁽⁴⁰⁾. Therefore, Si:H TFT devices reduce the efficiency of light transmittance and brightness. Besides, both amorphous and polycrystalline Si:H TFTs require relatively high process temperatures (350°C and 450°C , respectively)⁽⁴⁰⁾ making it difficult to fabricate these TFTs on plastics. One of

the methods to increase the efficiency and avoid high temperature is to use amorphous transparent oxides for the channels and electrodes, and fabricate TFTs at room temperature. Table 3-1 shows the major differences among amorphous IZO (α -IZO), amorphous Si (α -Si), and polycrystalline Si. Obviously, α -IZO has the advantages of high field effect mobility, high transparency, room temperature compatible processing, large area deposition by sputtering, plastics substrate available, and is a cheaper process⁽⁴⁰⁾.

TCOs are composed of post-transition metal oxides with outer major quantum number $n \geq 4$ ^(39,41). These TCOs exhibit n-type carriers^(122,123). Oxygen vacancies dominate the carrier concentration in these TCO films. For these TCOs, the mobility is high even in the amorphous film and close to that of polycrystalline film. It is very different from α -Si, which has an extremely low mobility ($<1 \text{ cm}^2/\text{Vs}$)⁽⁴⁰⁾ in amorphous type comparing to the several orders higher mobility in polycrystalline ($30\sim300 \text{ cm}^2/\text{Vs}$)⁽⁴⁰⁾ or in crystalline ($>1000 \text{ cm}^2/\text{Vs}$)⁽⁴⁰⁾. Table 2 shows that some commonly used TCOs have this feature. Although there is more than one mechanism explaining the conduction behavior for these TCOs, the most widely accepted theory of carrier transport is the ns orbitals overlapping of these transition metal atoms^(122,123). It was found only when the ns orbital overlap integral of the atomic metal wavefunction was large than 0.4, then the metal oxide can be conductive^(122,123). Although the study was based on the calculation of the crystalline metal oxide, it is still valid for amorphous films according to the observation from experimental measurements. Equation 3-1 describes the ns orbital's overlap integral.

$$S = \int \chi_i \cdot \chi_j dV \quad (3-1)$$

where χ_i and χ_j are Slater's atomic wavefunctions. Figure 3-1 shows the calculation results of

the ns orbital overlap integral for various metal oxides^(122,123). Below the value 0.4, metal oxides are very insulated while others are conductive with the value above 0.4. From table 3-2, it is very significant that carrier mobilities for those conductive oxides are not too much different between crystalline and amorphous films.

Among various conductive oxides, the IZO system exhibits many advantages such as high field effect mobility, high transparency, room temperature compatible process, large area deposition by sputtering, plastic substrates available, and is a cheaper process for transparent TFTs^(99,41,42,124,125). Other conductive oxides may not fit all the requirements for the flexible transparent TFTs. The first requirement is the film has to be transparent in visible region which means the bandgap $E_g > 3$ eV. CdO-PbO and AgSbO₃ systems have a bandgap smaller than this requirement^(126,127). The second requirement is the film must be amorphous and conductive as deposited in room temperature. CdO-CeO₂ is very resistive (resistivity $\sim 1 \times 10^4$ ohm-cm)⁽¹²⁸⁾ as deposited if no dopants are added in. In addition, Cd²⁺ ions are toxic against the environment⁽¹²²⁾. Amorphous In₂O₃ looks like a good candidate, however, when the oxygen ratio increases a little bit, it becomes polycrystalline^(123,129). ZnO is always polycrystalline as deposited⁽¹²⁵⁾. In₂O₃-ZnO systems have a wide range of amorphous materials in In/Zn ratio and various oxygen partial pressure^(130,122). Note that the change in oxygen ratio is very important because the carrier concentration can be adjusted by controlling the oxygen partial pressure or the O₂/Ar ratio. α -IZO has a considerable high mobility (10~50 cm²/Vs)^(41,125,40) as deposited at room temperature which is at least one order higher than amorphous Si⁽⁴⁰⁾. Ga₂O₃-ZnO (GZO) system has a little bit lower mobility than IZO⁽¹²⁵⁾. GaInZnO (GIZO) also has a little bit lower mobility compared to IZO⁽¹²²⁾. The last candidate is ITO, which is widely used as electrodes in LEDs, solar cells and LCDs^(131~133). Compared to ITO, IZO has a higher work function^(101,134,135), higher transmittance

in the infrared region⁽¹³⁶⁾, and lower In concentration than ITO⁽¹³⁴⁾. A higher In concentration means higher price⁽¹³⁴⁾. Accordingly, the IZO is selected to fabricate the TFTs in this research.

Table 3-1. Comparisons of materials for TFT used in display applications.

	α -IZO	α -Si	Poly-Si	Organics
Field Effect Mobility (cm ² /V-s)	10~50	0.5 ~ 1	30~300	0.1
Process Temperature (°C)	RT	~350	450	<150
Transparency (%)	>80	<20	<20	>80
Substrate	Glass/ Plastics	Glass	Quartz	Glass/Plastics

RT : room temperature, α -IZO : amorphous indium Zinc oxide, α -Si : amorphous Si, Poly-S : Polycrystalline Si

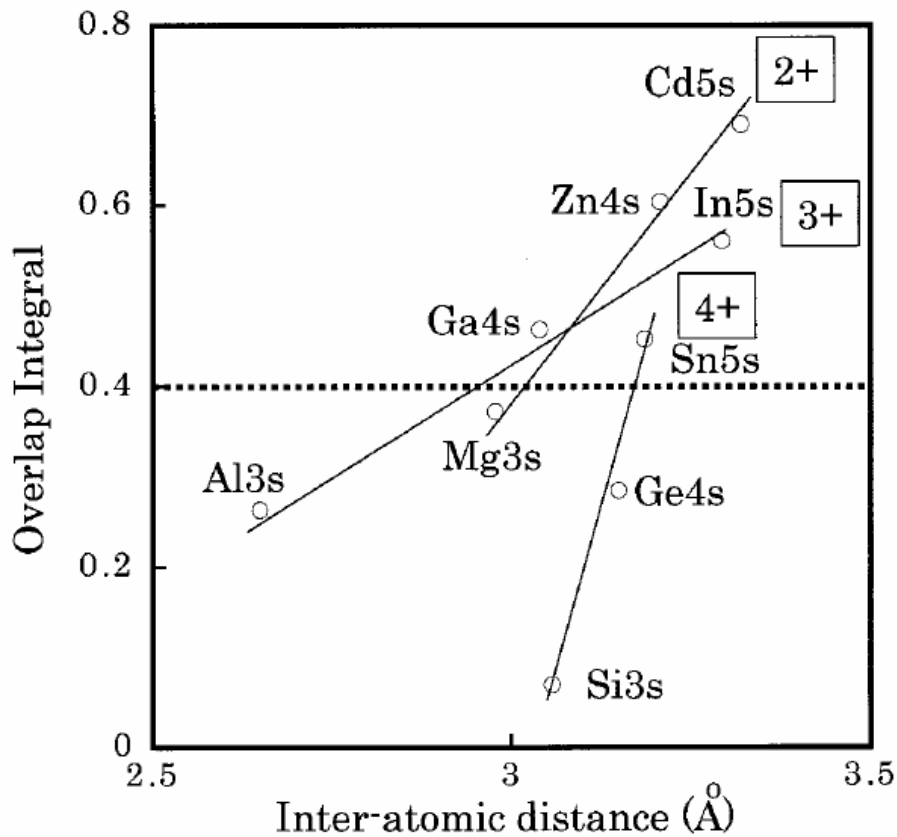


Figure 3-1. Wavefunction overlap integral of ns orbitals for various metal oxides.⁽¹²³⁾

Table 3-2. Comparisons of various conductive oxides.

Materials	Structure	Hall Mobility (cm ² /V-s)	Bandgap (eV)	Resistivity (Ω-cm)	Carrier Conc. (cm ⁻³)	Temp. (°C)	Reference
In ₂ O ₃	Amorph.	51	3.75	3x10 ⁻⁴	4.1x10 ²⁰	RT	123,129
In ₂ O ₃	Poly.	150		4x10 ⁻⁴	1x10 ²⁰	200	129
SnO ₂	Poly.	20.77	3.9~4.6	4.5x10 ⁻³	8.9x10 ¹⁹	150	137,138
ITO	Amorph.	27, 41	4.4	4.5~8x10 ⁻⁴	5x10 ²⁰	RT	139,140
ITO	Poly.	16, 53	4.3	5.46x10 ⁻⁴	7.1x10 ²⁰	RT/250	140
ZnO	Poly.	20	3.07~3.17	15.6	2x10 ¹⁶	RT	125
GaZnO	Amorph.	10	3.5~3.58	3x10 ⁻⁴	2x10 ²¹	RT	125
GaZnO	Single Cryst.	15~66	3.28	1.69x10 ⁻³	4x10 ¹⁹	900	141
InZnO	Amorph.	10~50	3.76~3.88	10 ⁻⁴ ~10 ⁻³	10 ²¹	RT	42,125
InZnO	Poly.	15~40		10 ⁻⁴ ~10 ⁻³	4~6x10 ²⁰	500	41
InGaO ₃ (ZnO)	Amorph.	21	3	3.85x10 ⁻³	7.7x10 ¹⁹	RT	122,123
2CdO-PbO ₂	Amorph.	9	1.85	5.7x10 ⁻³	1x10 ²⁰	RT	126
AgSbO ₃	Amorph.	6.7	2.3	3.45	2.7x10 ¹⁷	500	127
AbSbO ₃	Poly.	7.5		0.29	2.9x10 ¹⁸	675	127
2CdO-CeO ₂	Amorph.	10~12	3.4	4.76x10 ⁻³	1x10 ²⁰		128

RT : room temperature, Temp. : temperature, Amorph : amorphous, Poly. : polycrystalline, Cryst. : crystal., ITO : indium tin oxide,

3.2 Depletion Mode Indium Zinc Oxide Thin-Film Transistors

3.2.1 Experimental

The films were deposited on glass substrates (Corning EAGLE 2000) near room temperature by rf magnetron sputtering using 4 inch diameter targets of In₂O₃ and ZnO. The temperature at the substrate surface was ~ 40 °C after the *a*-IZO deposition, as determined from

temperature indicators attached to reference glass substrates. The working pressure was varied from 2-15 mTorr in a mixed ambient of O₂/Ar. The percentage of O₂ in the mixture was varied from 0-3%. At a percentage of 2.5 %, the film was obtained with carrier concentration of $\sim 10^{18}$ cm⁻³ and electron mobility of 17 cm².V⁻¹.s⁻¹ from Hall measurements. The partial pressure of oxygen during the sputter deposition was found to be the dominant factor controlling the conductivity of the films. The sputtering power on the targets was held constant at 125W, leading to compositions of the films measured by x-ray fluorescence spectroscopy of In/Zn=0.5 in atomic ratio. The typical thickness of the IZO films deposited was 150 nm, with a root mean square roughness of 0.4 nm measured over a 10x10 μm² area by Atomic Force Microscopy. The films were amorphous as determined by x-ray diffraction and showed optical transmittance of ~80% in the visible range.

Top-gate-type TFTs using a-IZO channels and 50 or 95-nm-thick SiO₂ gate insulators deposited by plasma enhanced chemical vapor deposition were fabricated as shown schematically in Figure 3-2 A). The SiO₂ layers were also deposited without heating the substrates, making the entire process consistent with typical continuous-use temperatures of commercial plastic films for electronic devices. Figure 3-2 B) also shows a plan-view optical micrograph of a TFT with a channel length (L) of 36 μm and a channel width (W) of 100 μm. The TFT structure was defined using photolithography and lift-off processes. The drain and source electrodes were formed with electron-beam evaporated Ti (2 nm)/Au (80 nm), which were defined by lithography on the *a*-IGZO films. Separate measurements of the specific contact resistance from linear transmission line measurements showed values of 8×10^{-5} Ω.cm² for these contacts without any annealing. The dc characteristics of the transistors were obtained using an Agilent 4145B parameter analyzer.

3.2.2 Results and Discussions

Figure 3-3 shows I_{DS} - V_{DS} characteristics from IZO transistors with 50 nm thick SiO_2 gate dielectric. The transistor operates in depletion-mode with an appreciable drain current at zero gate voltage and exhibits excellent drain current saturation. Note that the curves do not show any evidence of decreasing separation between I_D curves at larger currents. Such effects are commonly observed in oxide TFTs⁽⁹⁹⁾ and are attributed to either an electron injection barrier at the source contact or to mobility degradation due to interface roughness scattering as channel electrons are brought into closer proximity to the IZO/ SiO_2 interface.

Figure 3-4 shows I_{DS} and g_m as a function of V_{GS} for a device with 50 nm SiO_2 gate. The sub-threshold voltage swing was 1.9 V/decade and the device had a threshold voltage of -6.5V. The latter is the gate voltage at the onset of the initial sharp increase in current in a $\log(I_D)$ - V_{GS} characteristic. The drain current on-to-off ratio was $\sim 10^5$. These results are competitive with past results on TFTs using room temperature sputter deposited amorphous InGaZnO_4 as the channel material⁽⁴³⁾. The field-effect mobility was extracted from the ideal metal-oxide-semiconductor field effect transistor equation⁽⁴³⁾. A value of $\sim 4.5 \text{ cm}^2 \cdot \text{V}^{-1} \cdot \text{s}^{-1}$ was obtained, lower than the Hall mobility of $\sim 17 \text{ cm}^2 \cdot \text{V}^{-1} \cdot \text{s}^{-1}$ in the same layers. This is commonly observed in TFTs and suggests there is significant scattering of carriers by trapped charges at the IZO/ SiO_2 interface. A detailed discussion of the physical interpretations of mobility data extracted from oxide TFTs has been published previously⁽¹⁴²⁾. The extrinsic transconductance was 0.55 mS/mm.

The gate I-V characteristics from devices with two different gate dielectric thicknesses are shown in Figure 3-5. The leakage current is very small, in the 10^{-10} A range, for both gate thicknesses and demonstrates that the low temperature deposition process produces acceptable quality SiO_2 for TFT applications. The threshold voltage was decreased to -5.5V for the thicker

dielectric and the slope of the sub-threshold voltage swing was 0.87V/decade for the 95 nm thick dielectric.

3.2.3 Summary

In conclusion, IZO layers deposited at room temperature by sputtering is found to be a promising high mobility, *n*-type transparent TFT channel material. The IZO is amorphous under these conditions with excellent morphology and the TFTs operate in depletion mode with excellent on/off ratio. The low processing temperature suggests that IZO TFTs are promising for transparent or flexible electronics applications.

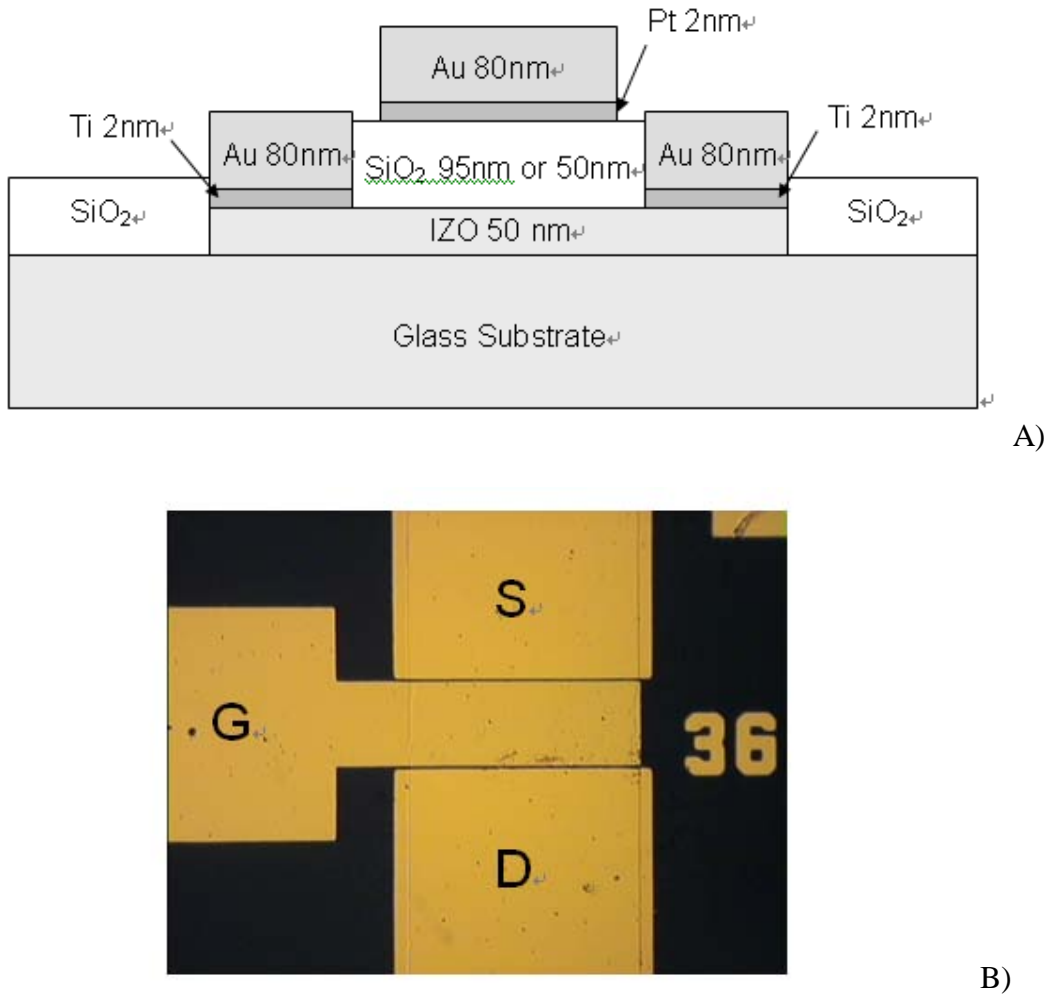


Figure 3-2. A depletion mode IZO TFT with SiO₂ gate dielectric. A) Schematic of the IZO TFT. B) SEM plan view of completed device.

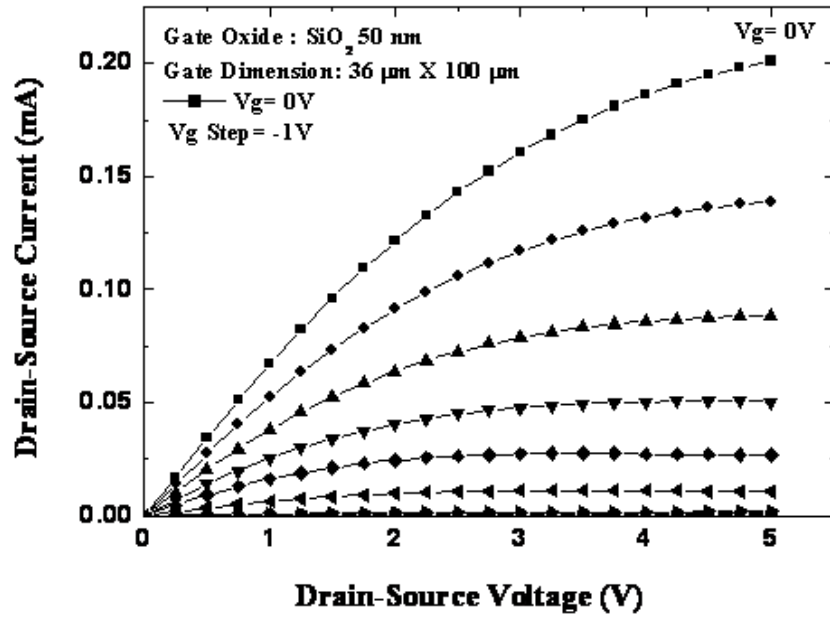


Figure 3-3. I_{DS} - V_{DS} characteristics at 0V gate bias from IZO transistors with 50 nm thick SiO₂ gate dielectric.

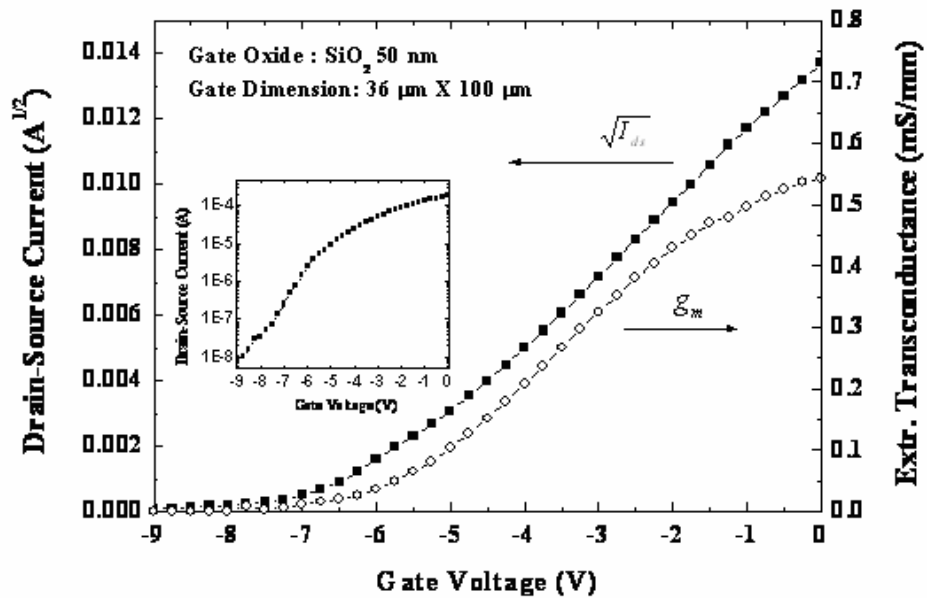


Figure 3-4. I_{DS} and g_m as a function of V_{GS} for a device with 50 nm SiO₂ gate (the inset shows the data in log-linear form).

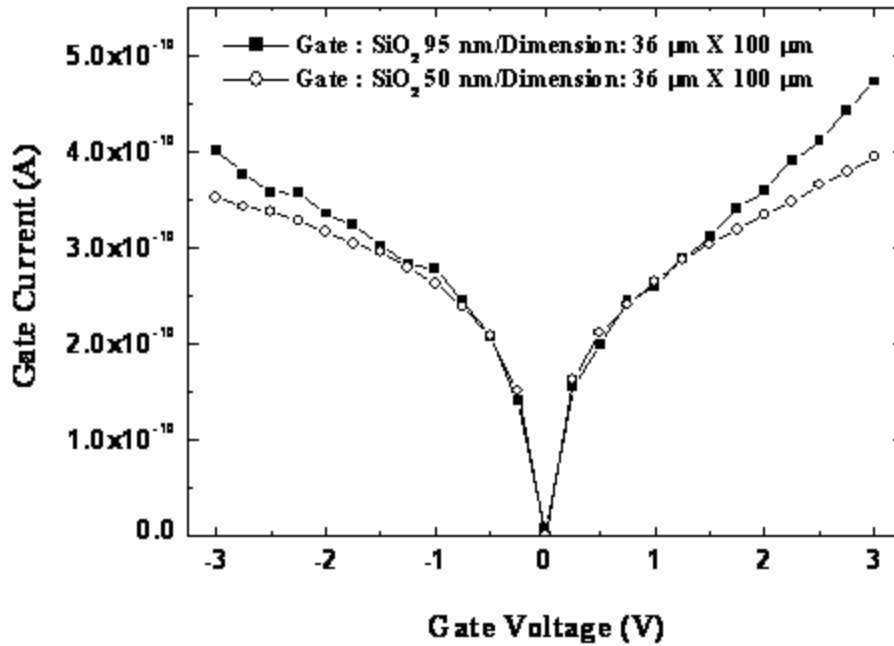


Figure 3-5. I_G - V_G for devices with two different SiO₂ gate dielectric thicknesses.

3.3 RF Characteristics of Small Gate Dimension of Depletion Mode Indium Zinc Oxide Thin-Film Transistors

3.3.1 Experimental

The films were deposited on glass substrates (Corning EAGLE 2000) near room temperature by rf magnetron sputtering using 4 inch diameter targets of In₂O₃ and ZnO. The temperature at the substrate surface was ~ 40 °C after the *a*-IZO deposition, as determined from temperature indicators attached to reference glass substrates. The working pressure was varied from 2-15 mTorr in a mixed ambient of O₂/Ar. The percentage of O₂ in the mixture was varied from 0-3%. At a percentage of 2.5 %, we obtained films with carrier concentration of ~10¹⁸ cm⁻³ and electron mobility of 17 cm².V⁻¹.s⁻¹ obtained from Hall measurements. The partial pressure of oxygen during the sputter deposition was found to be the dominant factor controlling the conductivity of the films. The sputtering power on the targets was held constant at 125W,

leading to compositions of the films measured by x-ray fluorescence spectroscopy of In/Zn=0.5 in atomic ratio. The typical thickness of the IZO films deposited was 150 nm, with a root mean square roughness of 0.4 nm measured over a $10 \times 10 \mu\text{m}^2$ area by Atomic Force Microscopy. The films were amorphous as determined by x-ray diffraction and showed optical transmittance of ~80% in the visible range.

Top-gate type TFTs using 50 nm of α -IZO channels and 12.5 nm-thick SiN_x gate insulators deposited by plasma enhanced chemical vapor deposition (PECVD) were fabricated as shown schematically in Figure 3-6 A). The SiN_x layer was also deposited without heating the substrates, making the entire process consistent with typical continuous-use temperatures of commercial plastic films for electronic devices. In addition, the SiN_x gate dielectric provided superior stability of device performance relative to SiO_2 deposited under the same conditions⁽¹⁴³⁾. Figure 3-6 B) also shows a plan-view optical micrograph of a double finger TFT with a gate dimension of $1 \mu\text{m} \times 200 \mu\text{m}$. The gate to source and drain distance are $0.5 \mu\text{m}$ and $1.0 \mu\text{m}$, respectively. The TFT structure was defined using photolithography and lift-off processes. The drain and source electrodes were formed with electron-beam evaporated Ti (20 nm)/Au (80 nm), which were defined by lithography on the α -IZO films. The Ti/Au metallization was also used as the final metal contact. Linear transmission line patterns were also fabricated on the same substrates. Specific contact resistance and sheet resistance from the linear transmission line measurements were $7 \times 10^{-5} \Omega \cdot \text{cm}^2$ and $0.9 \text{ M}\Omega/\text{sq}$, respectively. The dc characteristics of the transistors were obtained using an Agilent 4145B parameter analyzer and the rf measurements were conducted with an Agilent 8510 network analyzer.

3.3.2 Results and Discussions

Figure 3-7 shows typical drain current versus drain voltage, I_{DS} - V_{DS} , characteristics from the IZO transistors. The transistor operates in depletion-mode with an appreciable drain current of 2 mA/mm at zero gate voltage. Figure 3-8 A) shows drain current, I_{DS} , and transconductance, g_m , as a function of V_{GS} for an IZO TFT. A maximum transconductance of 7.5 mS/mm was obtained at $V_{ds}=3V$ and $V_g=0V$ and this is the highest transconductance ever reported for IZO based TFTs^(143,16,17). The transistor has a threshold voltage of -2.5V, which is the gate voltage at the onset of the initial sharp increase in current in a $\log(I_D)$ - V_{GS} characteristic. The field-effect mobility was extracted from the ideal metal–oxide–semiconductor field effect transistor equation in the saturation region⁽⁴³⁾. A value of $14.5 \text{ cm}^2 \cdot \text{V}^{-1} \cdot \text{s}^{-1}$ was obtained, only slightly lower than the Hall mobility of $\sim 17 \text{ cm}^2 \cdot \text{V}^{-1} \cdot \text{s}^{-1}$ in the thicker film of the same layers. This reduced value of field mobility relative to Hall mobility is commonly observed in TFTs and suggests that there is some scattering of carriers by trapped charges at the IZO/SiN_x interface. A detailed discussion of the physical interpretations of the various types of mobilities extracted from oxide TFTs has been published previously in an IGO based TFT paper⁽¹⁴²⁾. The drain and gate current are also plot in logarithmic scale verses gate voltage, as shown in Figure 3-8 B). The gate leakage current is 2×10^{-10} A and the drain current on-to-off ratio is $>10^5$.

The measured s-parameters, estimated h_{21} and unilateral power gain of a typical IZO TFT are illustrated in Figure 3-9. The TFT was biased at drain and gate voltage of 3V and 0V, respectively during the s-parameter measurements. Unity gain cut-off frequency and maximum frequency of oscillation of 180 and 155 MHz, respectively, were achieved. A simplified equivalent T-model for the IZO TFT, as shown in Figure 3-10, was used to extract the device parameters. The extracted device parameters are listed in Table 3-3. The extracted source and

drain resistance were consistent with the estimated resistance based on the transmission line measurements and drain I-V characteristics. The simulated intrinsic transconductance was very close to the measured extrinsic transconductance. The low cut-off frequency of the IZO was limited by the fairly long transit time, 16 ps, low transconductance, and high parasitic resistances, which were resulted from low mobility and saturation velocity of the α -IZO channel layer. However, this MHz range switching performance is sufficient for many display applications.

3.3.3 Summary

In conclusion, dc and rf characteristics of small gate length IZO TFTs were measured. A T-model was used to extract the device parasitic parameters. This is the first report of rf performance for IZO TFTs. The transistor showed good dc performance. An extrinsic transconductance of 7.5 mS/mm was achieved, which is the highest ever reported. The IZO thin film deposition and transistor fabrication were performed at room temperature, which makes this technology suitable for applications on flexible organic substrates.

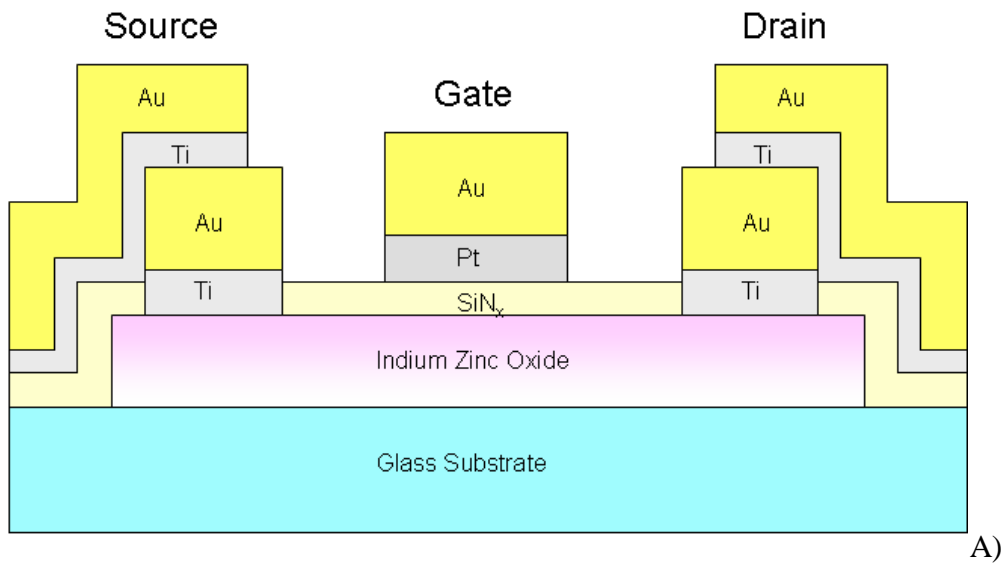
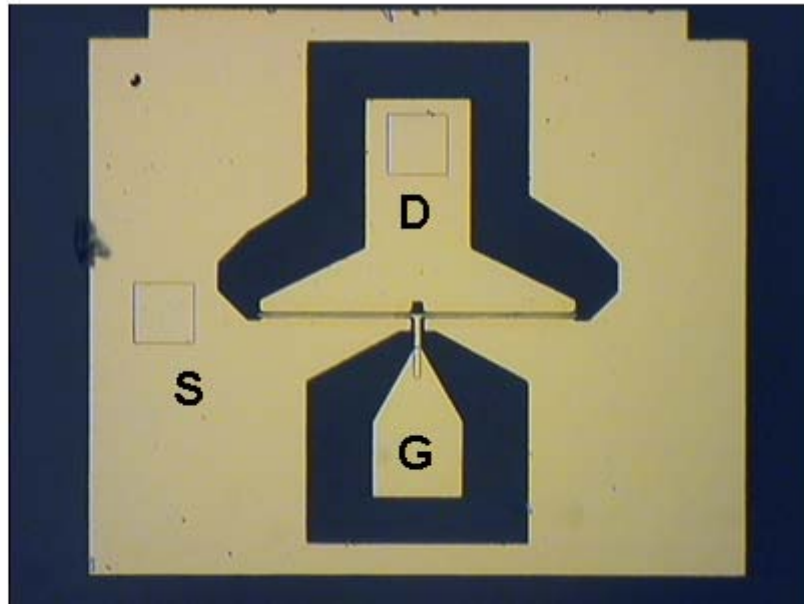


Figure 3-6. An depletion mode IZO TFT with SiN_x gate dielectric A) Schematic of the TFT. B) optical microscopy plan view of the TFT.



B)

Figure 3-6. Continued

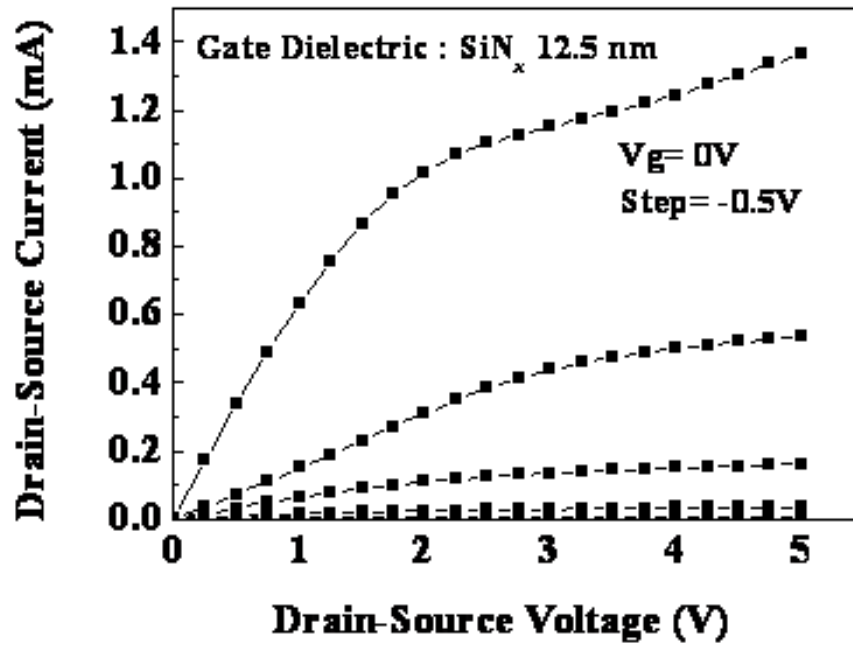
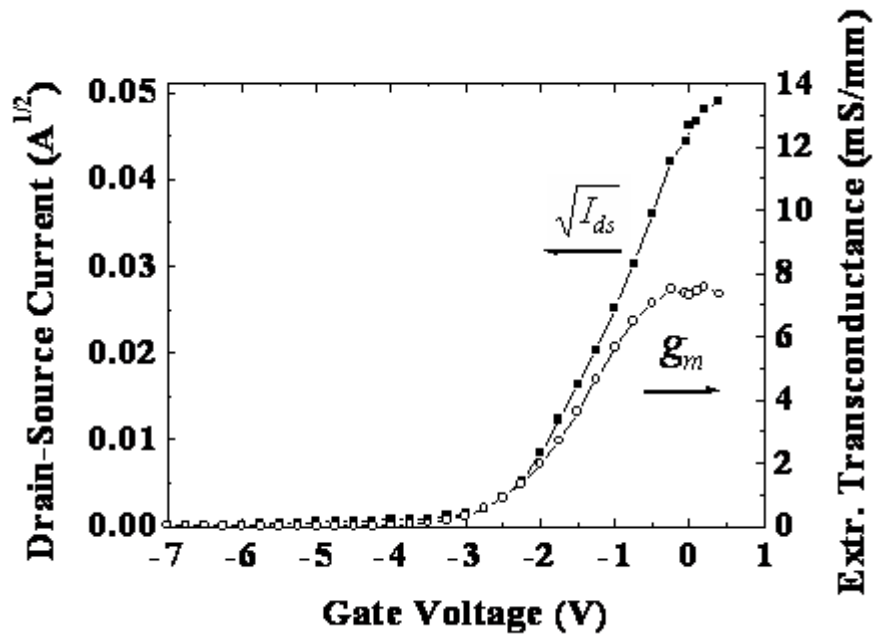
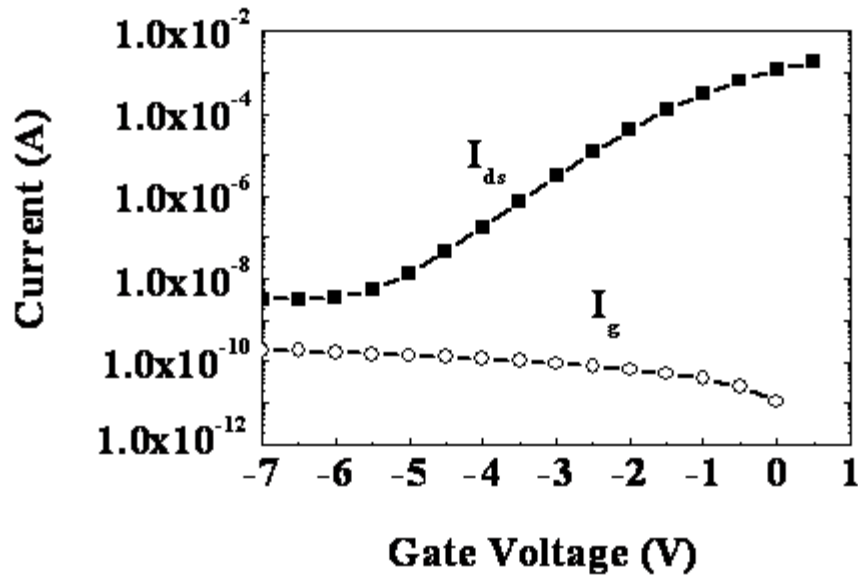


Figure 3-7. I_{ds} - V_{ds} characteristics of a typical depletion mode IZO TFT with gate-dimension of $1 \mu\text{m} \times 200 \mu\text{m}$.

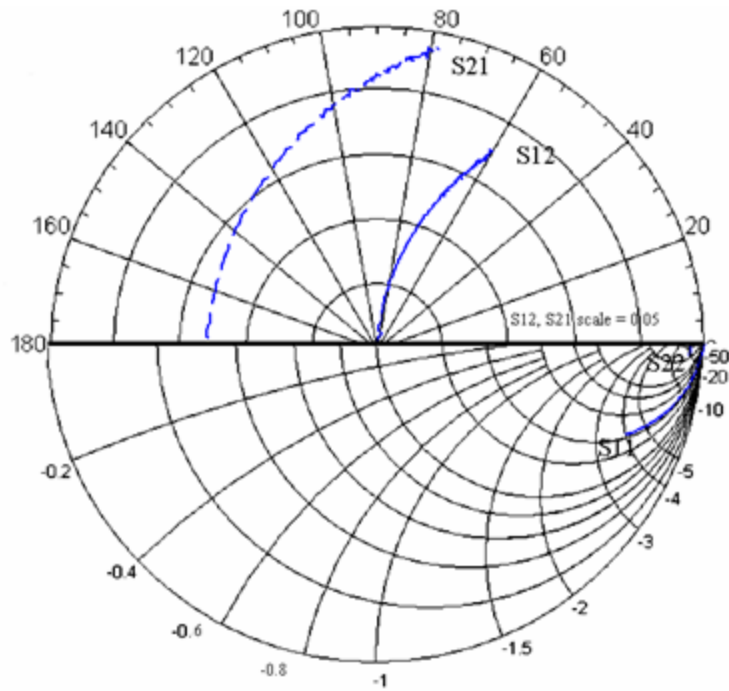


A)

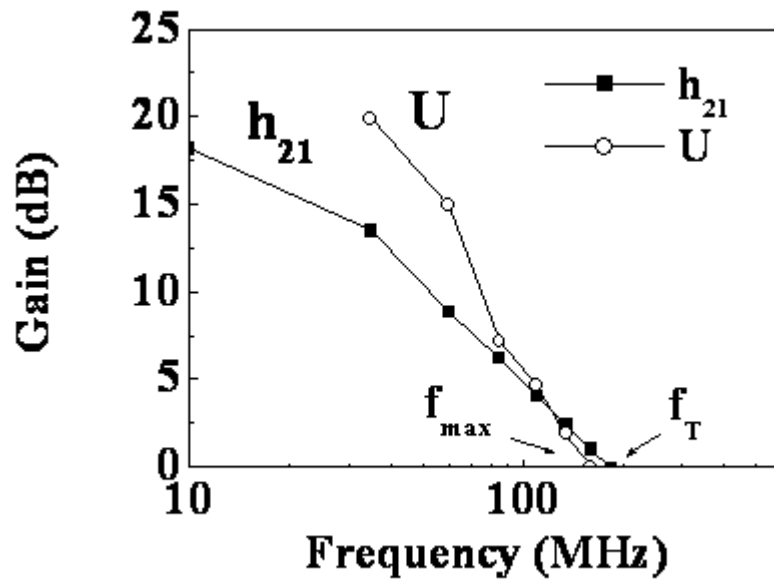


B)

Figure 3-8. DC characteristics of a typical depletion mode IZO TFT. A) I_{ds} and g_m as a function of V_{gs} at $V_{ds}=3$ V. B) The logarithmic scale of I_{ds} and I_g versus V_g of the same device.



A)



B)

Figure 3-9. RF characteristics of a depletion mode IZO TFT. A) Measured s-parameters of a $1 \mu\text{m} \times 200 \mu\text{m}$ gate-dimension of a depletion mode IZO TFT biased at $V_{ds} = 3 \text{ V}$ and $V_{gs} = 0 \text{ V}$. B) Calculated h_{21} and unilateral power gain based on measured s-parameters.

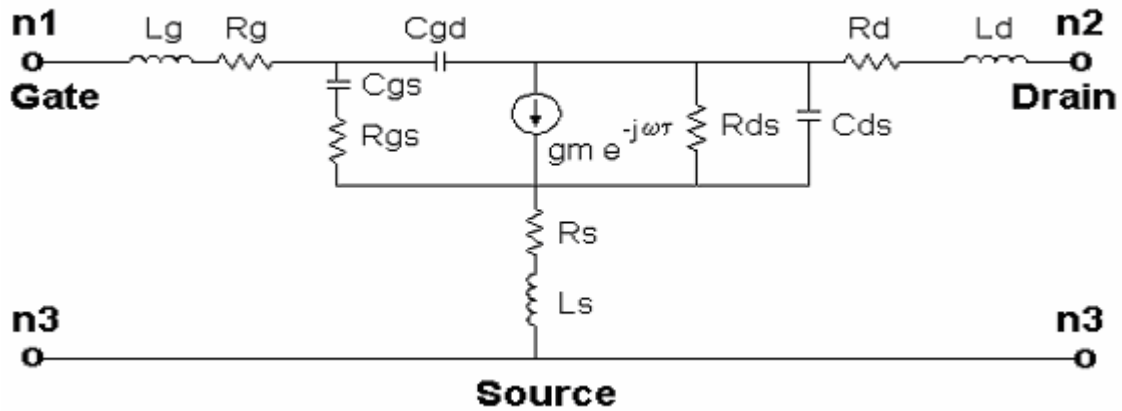


Figure 3-10. A simplified equivalent circuit of IZO TFT.

Table 3-3. Extracted device parasitic parameters using a T-model.

Parameters	Value
g_m (mS)	1.4
C_{gs} (pF)	0.26
R_{ds} (Ω)	270
C_{ds} (pF)	0.01
C_{dg} (pF)	0.11
R_{gs} (Ω)	86
R_g (Ω)	17
R_s (Ω)	40
R_d (Ω)	1100
τ (pS)	16
L_g (nH)	0.01
L_s (nH)	1.7
L_d (nH)	0.03

3.4 Enhancement Mode Indium Zinc Oxide Thin-Film Transistors

3.4.1 Experimental

To fabricate enhancement mode IZO TFTs, the carrier concentration was determined by selecting a higher O_2/Ar ratio for sputtering condition. The films were deposited on glass substrates (Corning EAGLE 2000) near room temperature by rf magnetron sputtering using 4 inch diameter targets of In_2O_3 and ZnO. The temperature at the substrate surface was ~ 40 °C after the *a*-IZO deposition, as determined from temperature indicators attached to reference glass

substrates. The working pressure was varied from 2-15 mTorr in a mixed ambient of O₂/Ar. The percentage of O₂ in the mixture was varied from 0-3%. At a percentage of 3.1 %, we obtained films with carrier concentration of $1.5 \times 10^{16} \text{ cm}^{-3}$ and electron mobility of $10 \sim 20 \text{ cm}^2 \cdot \text{V}^{-1} \cdot \text{s}^{-1}$ obtained from Hall measurements. The partial pressure of oxygen during the sputter deposition was found to be the dominant factor controlling the conductivity of the films. The sputtering power on the targets was held constant at 125W, leading to compositions of the films measured by x-ray fluorescence spectroscopy of In/Zn=0.5 in atomic ratio. The typical thickness of the IZO films deposited was 150 nm, with a root mean square roughness of 0.4 nm measured over a $10 \times 10 \mu\text{m}^2$ area by Atomic Force Microscopy. The films were amorphous as determined by x-ray diffraction and showed optical transmittance of ~80% in the visible range.

Top-gate-type TFTs using 20nm of a-IZO channels and 100-nm-thick SiO₂ gate insulators deposited by PECVD were fabricated as shown schematically in Figure 3-11 A). The SiO₂ layers were also deposited without heating the substrates, making the entire process consistent with typical continuous-use temperatures of commercial plastic films for electronic devices. Figure 3-11 B) also shows a plan-view optical micrograph of a TFT with a channel length (L) of $1 \mu\text{m}$ and a channel width (W) of $2 \times 100 \mu\text{m}$. The TFT structure was defined using photolithography and lift-off processes. The drain and source electrodes were formed with electron-beam evaporated Ti (2 nm)/Au (80 nm), which were defined by lithography on the *a*-IGZO films. The dc characteristics of the transistors were obtained using an Agilent 4145B parameter analyzer.

3.4.2 Results and Discussions

Figure 3-12 shows $I_{\text{DS}}-V_{\text{DS}}$ characteristics from IZO transistors. The transistor operates in enhancement-mode with an appreciable drain current after turn-on and exhibits excellent drain current saturation. The transistor can also pinch off nicely.

Figure 3-13 (a) shows I_{DS} and g_m as a function of V_{GS} for the TFT. The sub-threshold voltage swing was 0.253 V/decade and the device had a threshold voltage of 0.75V. Figure 3-13 B) is the gate voltage at the onset of the initial sharp increase in current in a $\log(I_D)-V_{GS}$ characteristic. The drain current on-to-off ratio was $>10^6$. These results are competitive with past results on TFTs using room temperature sputter deposited amorphous InGaZnO₄ as the channel material⁽²²⁾. The field-effect mobility was extracted from the ideal metal–oxide–semiconductor field effect transistor equation⁽⁴³⁾. A high field-effect mobility value of $39.7 \text{ cm}^2 \cdot \text{V}^{-1} \cdot \text{s}^{-1}$ was obtained. The gate leakage current is very small, in the 10^{-10} A range, as shown in the inset data of Figure 3-13 B).

3.4.3 Summary

In conclusion, enhancement mode TFTs with IZO channel layers deposited at room temperature by sputtering was fabricated. These TFTs show high mobility and high transparency, making them suitable for high resolution displays. The low processing temperature of the IZO TFTs suggests that they are promising for transparent or flexible electronics applications.

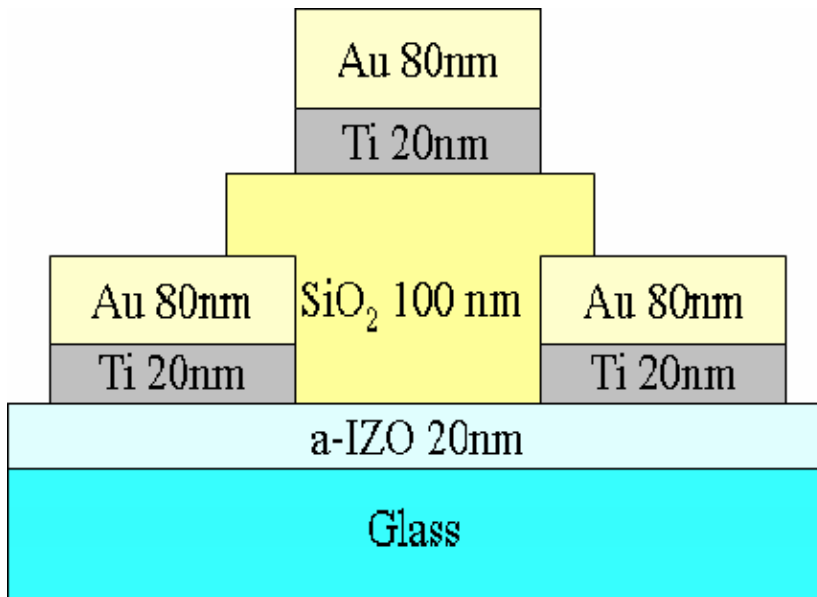


Figure 3-11. Schematic of an enhancement mode IZO-TFT.

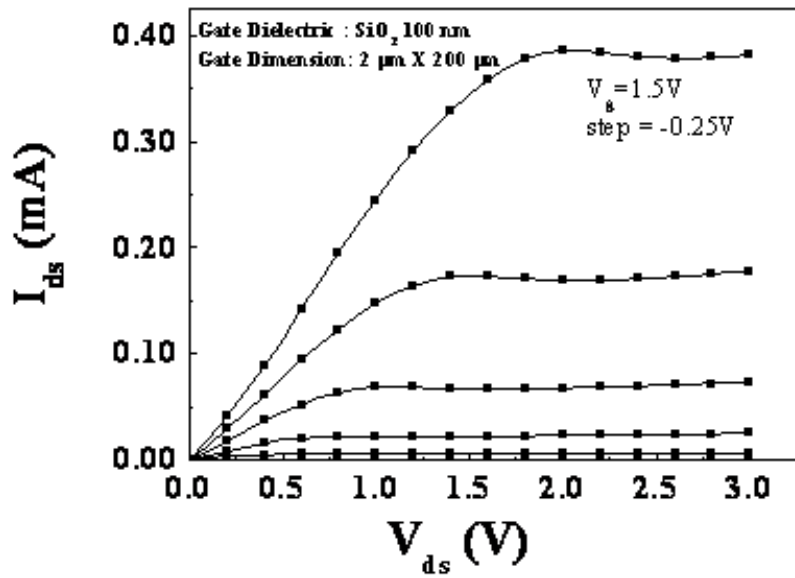
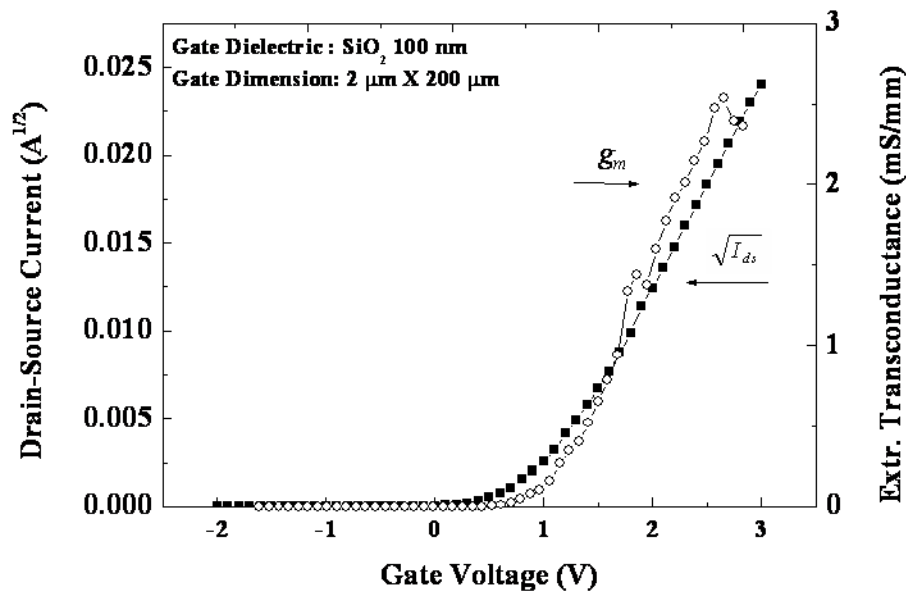
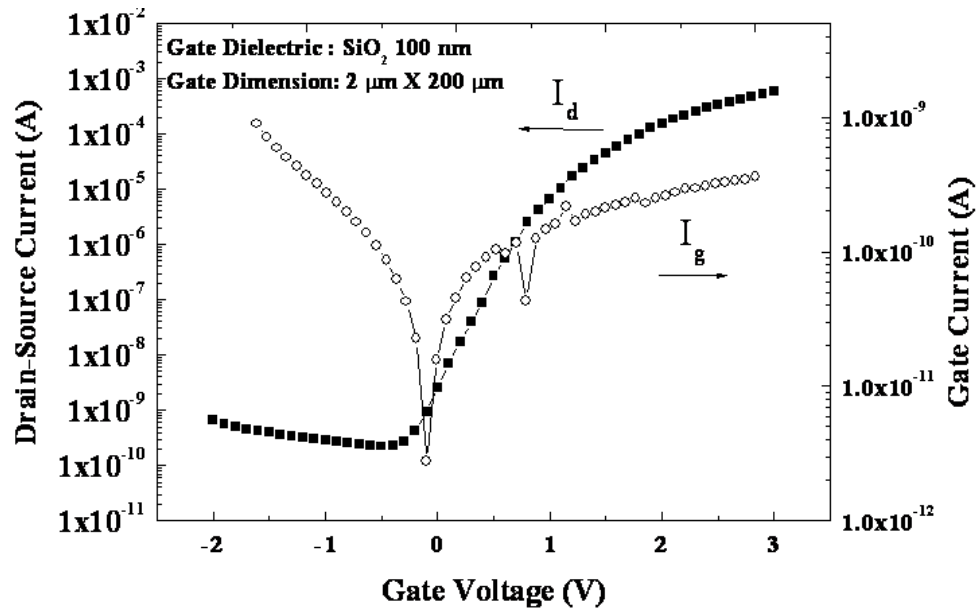


Figure 3-12. I_{ds} - V_{ds} characteristics of an enhancement IZO TFT with gate-dimension of $2\ \mu\text{m} \times 200\ \mu\text{m}$.



A)

Figure 3-13. Graph characteristics for enhancement mode IZO TFT measured at $V_{ds}=2\text{V}$. A) I_{ds} and g_m as a function of V_{gs} . B) The logarithmic scale of I_{ds} and I_g versus V_g .



B)

Figure 3-13. Continued

CHAPTER 4
ALGAN/GAN HIGH ELECTRON MOBILITY TRANSISTOR-BASED BIOSENSORS

4.1 Background

AlGa_N/Ga_N high electron mobility transistors (HEMTs) have shown promise for bio-sensing applications⁽⁶²⁻⁶⁷⁾, since they include a high electron sheet carrier concentration channel induced by piezoelectric polarization of the strained AlGa_N layer and spontaneous polarization⁽⁶²⁻⁷⁵⁾. There are positive counter charges at the HEMT surface layer induced by the electrons located at the AlGa_N/Ga_N interface. Any slight changes in the ambient can affect the surface charge of the HEMT, thus changing the electron concentration in the channel at AlGa_N/Ga_N interface.

Biological weapons are particularly attractive tools for terror because biological agents are available and easy to manufacture, small amounts are required to cause large-scale effects, and attacks can easily overwhelm existing medical resources. Reliable detection of biological agents in the field and in real time has proved to be challenging. Clostridium botulinum neurotoxins are among the more deadly toxins and are listed as a NIAID—Category A agent for bioterrorism potential. The lethal dose in unvaccinated humans is estimated at 1 ng/kg^(46,47). Conventional methods of detection involve the use of HPLC, mass spectrometry and colorimetric ELISAs; but these are impractical because such tests can only be carried out at centralized locations, and are too slow to be of practical value in the field⁽⁴⁸⁻⁶⁰⁾. Another test for botulinum toxin detection is the ‘mouse assay’, which relies on the death of mice as an indicator of toxin presence⁽¹⁶⁾. Clearly, such methods are slow and impractical in the field.

Perkinsus species (Perkinsozoa, Alveolata) are the causative agent of perkinsosis in a variety of mollusc species. Perkinsus species infections cause widespread mortality in both natural and farmed oyster populations, resulting in severe economic loss for the shellfishery, and

detrimental effects on the environment⁽⁷⁶⁻⁸⁰⁾. Currently, the standard diagnostic method for Perkinsus species infections has been the fluid thioglycollate medium (FTM) assay detection. However, it takes several days to do the detection⁽⁸¹⁾. Polymerase chain reaction (PCR)-based technique is also used to determine the Perkinsus species but it is more expensive, time-consuming, and requires exquisite controls to assure specificity and accuracy⁽⁸²⁾. Clearly, such methods are slow and impractical in the field.

In this study, antibody-functionalized Au-gated AlGaN/GaN high electron mobility transistors (HEMTs) were used for detecting botulinum toxin in buffer solution and Perkinsus Marinus (*P. marinus*) in sea waters, respectively. The botulinum toxin was specifically recognized through anti-botulinum antibody, anchored to the gate area. The range of concentration from 0.1 ng/ml to 100 ng/ml of botulinum was investigated. Waters from tanks in which *Tridacna crocea* were living and dead were tested for the existence of *P. marinus*. The *P. marinus* was also recognized through the anti-*P. marinus* antibody, anchored to the gate area. We demonstrated the *P. marinus* detection for field-deployable or potable sensor applications.

4.2 Botulinum Neurotoxin Biosensor

4.2.1 Experimental

The HEMT structures consisted of a 3 μm thick undoped GaN buffer, 30 \AA thick $\text{Al}_{0.3}\text{Ga}_{0.7}\text{N}$ spacer, 220 \AA thick Si-doped $\text{Al}_{0.3}\text{Ga}_{0.7}\text{N}$ cap layer. The epi-layers were grown by a molecular beam epitaxy system (MBE) on sapphire substrates. Mesa isolation was performed with an Inductively Coupled Plasma (ICP) etching with Cl_2/Ar based discharges at -90 V dc self-bias, ICP power of 300 W at 2 MHz and a process pressure of 5 mTorr. $10 \times 50 \mu\text{m}^2$ Ohmic contacts separated with gaps of 5 μm consisted of e-beam deposited Ti/Al/Pt/Au patterned by lift-off and annealed at 850 $^\circ\text{C}$, 45 sec under flowing N_2 . 400-nm-thick 4% Polymethyl Methacrylate (PMMA) was used to encapsulate the source/drain regions, with only the gate

region open to allow the liquid solutions to cross the surface. The source-drain current-voltage characteristics were measured at 25°C using an Agilent 4156C parameter analyzer with the gate region exposed.

Figure 4-1 shows a schematic device cross sectional view with the immobilized thioglycolic acid, followed by botulinum antibody coating. The Au surface was functionalized with the specific bi-functional molecule, thioglycolic acid. We anchored a self-assembled monolayer of thioglycolic acid, HSCH₂COOH, an organic compound and containing both a thiol (mercaptan) and a carboxylic acid functional group, on the Au surface in the gate area through strong interaction between gold and the thiol-group of the thioglycolic acid. The devices were first placed in the oxygen plasma chamber and then submerged in 1 mM aqueous solution of thioglycolic acid at 4 °C. This resulted in binding of the thioglycolic acid to the Au surface in the gate area with the COOH groups available for further chemical linking of other functional groups. X-Ray Photoelectron Spectroscopy and electrical measurements confirming a high surface coverage and Au-S bonding formation on the GaN surface have been previously published⁽⁷³⁾. The device was incubated in a phosphate buffered saline (PBS) solution of 200 μg/ml botulinum polyclonal rabbit antibody for 18 hours before real time measurement of botulinum toxin subtype A acquired from Metabionics Inc.

After incubation with a PBS buffered solution containing botulinum antibody at a concentration of 200 μg/ml, the device surface was thoroughly rinsed off with PBS and dried by a nitrogen blower. The source and drain current from the HEMT were measured before and after the sensor was exposed to 100 ng/ml of botulinum toxin at a constant drain bias voltage of 500 mV, as shown in Figure 4-2 A). Any slight changes in the ambient of the HEMT affect the surface charges on the AlGaN/GaN. These changes in the surface charge are transduced into a

change in the concentration of the 2DEG in the AlGaIn/GaN HEMTs, leading to the decrease in the conductance for the device after exposure to botulinum toxin.

4.2.2 Results and Discussions

Figure 4-2 B) shows a real time botulinum toxin detection in PBS buffer solution using the source and drain current change with constant bias of 500 mV. No current change can be seen with the addition of buffer solution around 100 seconds, showing the specificity and stability of the device. In clear contrast, the current change showed a rapid response in less than 5 seconds when target 1 ng/ml botulinum toxin was added to the surface. The abrupt current change due to the exposure of botulinum toxin in a buffer solution was stabilized after the botulinum toxin thoroughly diffused into the buffer solution. Different concentrations (from 0.1 ng/ml to 100 ng/ml) of the exposed target botulinum toxin in a buffer solution were detected. The sensor saturates above 10ng/ml of the toxin. The experiment at each concentration was repeated four times to calculate the standard deviation of source-drain current response. The limit of detection of this device was below 1 ng/ml of botulinum toxin in PBS buffer solution. The source-drain current change was nonlinearly proportional to botulinum toxin concentration, as shown in Figure 4-3. Figure 4-4 shows a real time test of botulinum toxin at different toxin concentrations with intervening washes to break antibody-antigen bonds. This result demonstrates the real-time capabilities and recyclability of the chip. Moreover, Figure 4-5 shows the real-time test at room temperature of a used botulinum sensor, which had been stored in PBS (pH 7.4) at 4°C for three months, still showed a very good sensitivity and reproducibility.

4.2.3 Summary

In summary, it has been shown that through a chemical modification method, the Au-gated region of an AlGaIn/GaN HEMT structure can be functionalized for the detection of botulinum

toxin with a limit of detection less than 1 ng/ml. This botulinum sensor did not only have a low detection limit but also can be recycled and has a long term stability, sensitivity and reliability. This electronic detection of biomolecules is a significant step towards a field-deployed sensor chip, which can be integrated with a commercial available wireless transmitter to realize a real-time, fast response and high sensitivity botulinum toxin detector.

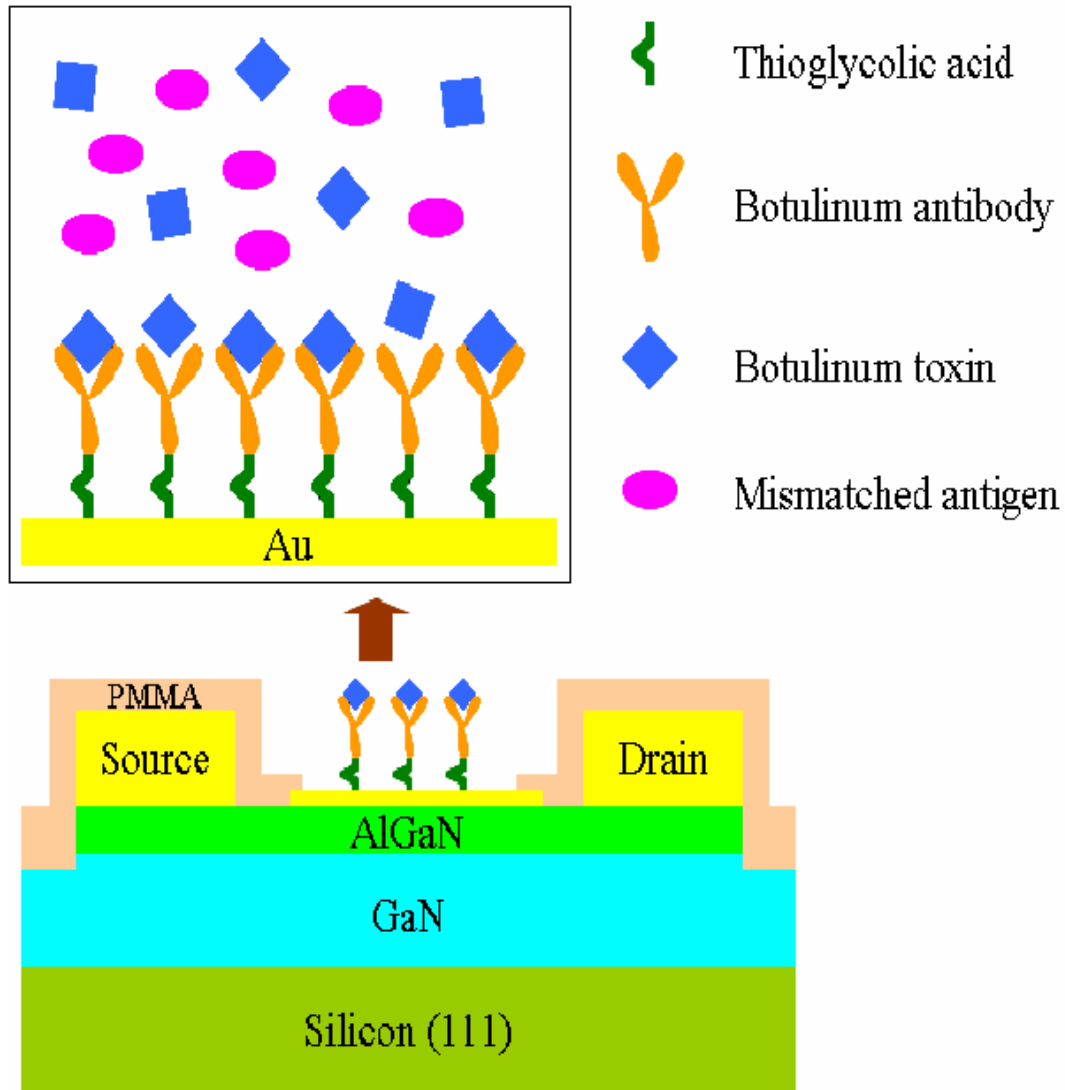
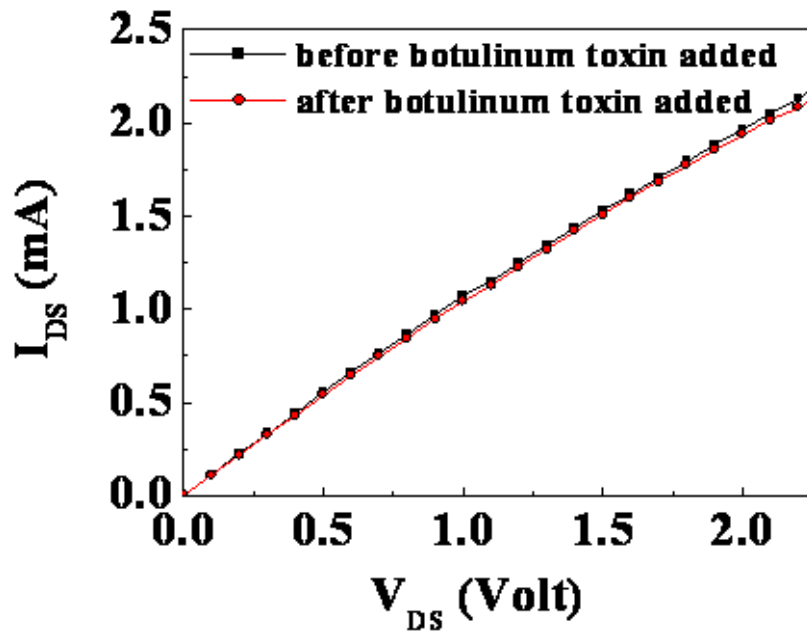
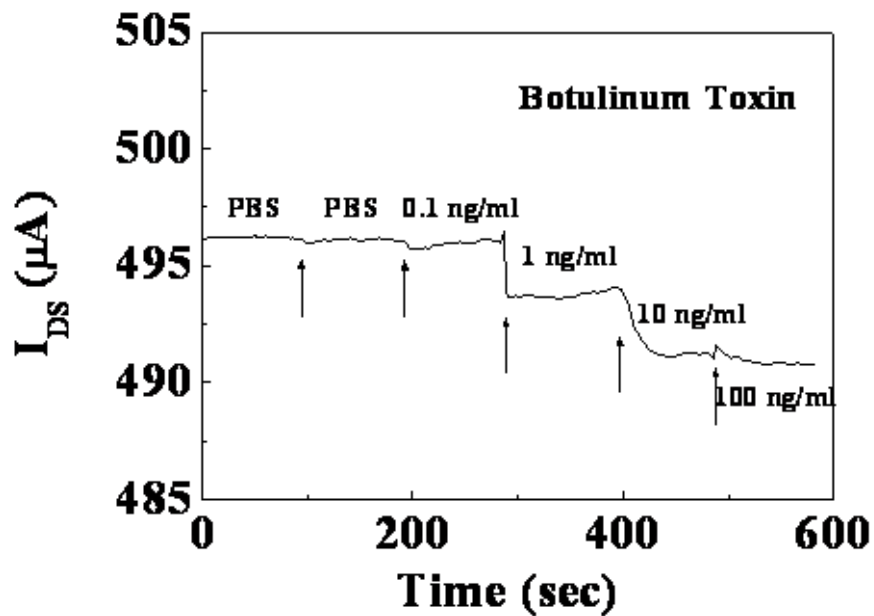


Figure 4-1. Schematic of AlGaN/GaN HEMT sensor. The Au-coated gate area was functionalized with anti-botulinum antibody/ botulinum antigen on thioglycolic acid



A)



B)

Figure 4-2. DC response of the antibody-functionalized AlGaIn/GaN HEMT to botulinum toxin
 A) I-V characteristics of AlGaIn/GaN HEMT sensor before and after exposure to 100ng/ml botulinum toxin. B) Drain current of an AlGaIn/GaN HEMT versus time for botulinum toxin from 0.1 ng/ml to 100 ng/ml.

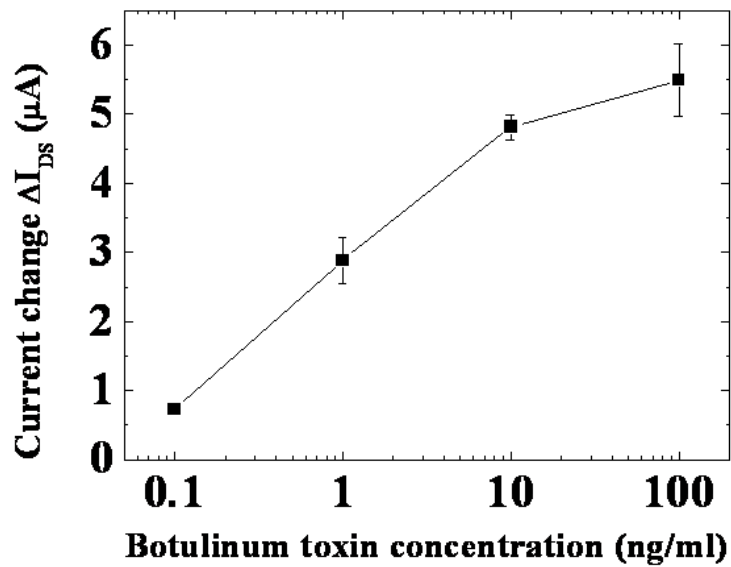


Figure 4-3. Change of drain current versus different concentrations from 0.1 ng/ml to 100 ng/ml of botulinum toxin.

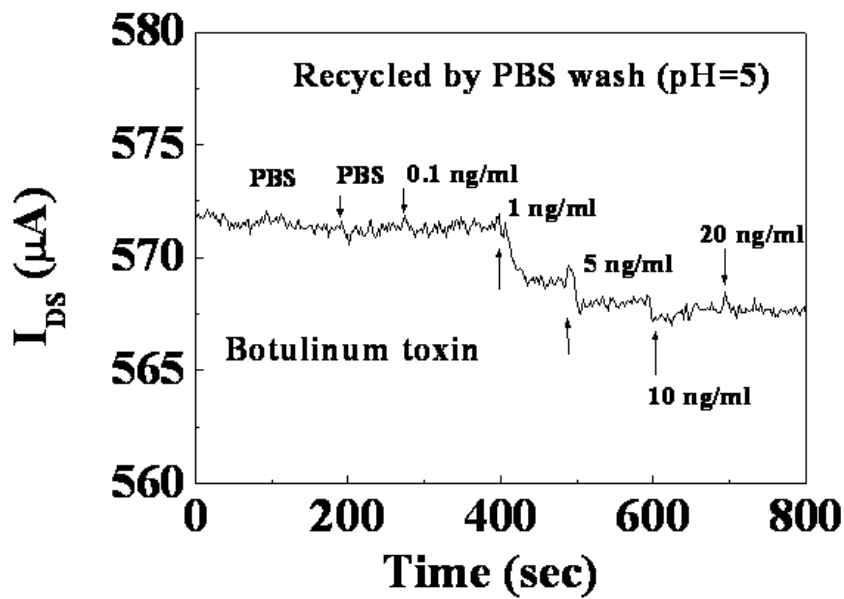


Figure 4-4. The real-time test from a used sensor which was washed with PBS in pH 5 to refresh the sensor.

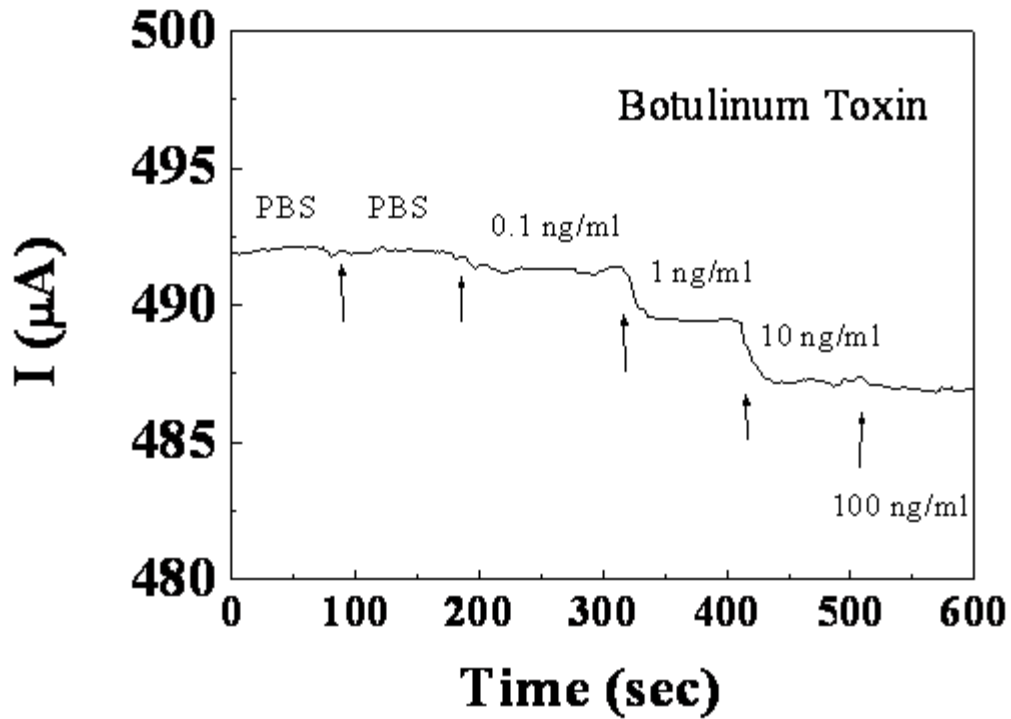


Figure 4-5. The real-time test from a used sensor which had been fabricated for 3 months.

4.3 Perkinsus Marinus Biosensors

4.3.1 Experimental

5nm thickness of Au was deposited on the gate area of the AlGaN/GaN HEMT. The HEMT structures consisted of a 3 μm thick undoped GaN buffer, 180 \AA thick un-doped $\text{Al}_{0.26}\text{Ga}_{0.74}\text{N}$ cap layer. The epi-layers were grown by a molecular beam epitaxy system (MBE) on Si substrates. Mesa isolation was performed with an Inductively Coupled Plasma (ICP) etching with Cl_2/Ar based discharges at -90 V dc self-bias, ICP power of 300 W at 2 MHz and a process pressure of 5 mTorr. $10 \times 50 \mu\text{m}^2$ Ohmic contacts separated with gaps of 5 μm consisted of e-beam deposited Ti/Al/Pt/Au patterned by lift-off and annealed at 850 $^\circ\text{C}$, 45 sec under flowing N_2 . 400-nm-thick 4% Polymethyl Methacrylate (PMMA) was used to encapsulate the source/drain regions, with only the gate region open to allow the liquid solutions to cross the

surface. The source-drain current-voltage characteristics were measured at 25°C using an Agilent 4156C parameter analyzer with the gate region exposed.

Figure 4-6 shows a schematic device cross sectional view with the immobilized thioglycolic acid, followed by anti-*P. marinus* antibody coating. The Au surface was functionalized with the specific bi-functional molecule, thioglycolic acid. A self-assembled monolayer of thioglycolic acid, HSCH₂COOH, an organic compound and containing both a thiol (mercaptan) and a carboxylic acid functional group, was anchored on the Au surface in the gate area through strong interaction between gold and the thiol-group of the thioglycolic acid. The devices were first placed in the oxygen plasma chamber and then submerged in 1 mM aqueous solution of thioglycolic acid at 4 °C. This resulted in binding of the thioglycolic acid to the Au surface in the gate area with the COOH groups available for further chemical linking of other functional groups. X-Ray Photoelectron Spectroscopy and electrical measurements confirming a high surface coverage and Au-S bonding formation on the GaN surface have been previously published⁽⁷³⁾. The device was incubated in a phosphate buffered saline (PBS) solution of 200 μg/ml anti-*P. marinus* rabbit antibody for 18 hours before real time measurement of the infected waters.

After incubation with a PBS buffered solution containing anti-*P. marinus* antibody at a concentration of 200 μg/ml, the device surface was thoroughly rinsed off with PBS and dried by a nitrogen blower. The source and drain current from the HEMT were measured at a constant drain bias voltage of 500 mV before and after the sensor was exposed to the water from the tank 1 that the clams died, as shown in Figure 4-7 A). Any slight changes in the ambient of the HEMT affect the surface charges on the AlGaN/GaN. These changes in the surface charge are

transduced into a change in the concentration of the 2DEG in the AlGaIn/GaN HEMTs, leading to the decrease in the conductance for the device after exposure to botulinum toxin.

4.3.2 Results and Discussions

Figure 4-7 B) shows a real time *P. marinus* detection in PBS buffer solution using the source and drain current change with constant bias of 500 mV. No current change can be seen with the addition of buffer solution around 100 seconds, showing the specificity and stability of the device. In clear contrast, the current change showed a rapid response in less than 5 seconds when 2ul of tank 1 water was added to the surface. The abrupt current change due to the exposure of *P. marinus* in a buffer solution was stabilized after the antigen thoroughly diffused into the buffer solution. Continuous drops of the tank 1 water into a buffer solution were detected. The sensor saturates after several drops were added. Obviously, in tank 1, clams died and some *P. marinus* cells also died and release the specific antigens that were detected by the sensors. Figure 4-8 shows the real-time detection of the original water, in which the clams were alive. De-ionized water was intentionally added into the PBS on the sensor and there is no any current change. Once the original water was added, the sensor shows current drops. When more drops were added, the current continuously dropped. This indicates that very diluted concentration of specific antigens from the *P. marinus* were released into the original water. Before conducting the experiment, the original water was frozen at -70°C to kill the *P. marinus* cells. This might be the easier way to extract the antigens from the cells. Figure 4-9 A) shows a real time test of *P. marinus* in the water from tank 2. The sensor was then washed with PBS (pH 7.4) and used to detect the *P. marinus* again. The recycled sensor still shows very good sensitivity as previously, shown as Figure 4-9 B). This result demonstrates the real-time capabilities and recyclability of this sensor.

4.3.3 Summary

In summary, the Au-gated region of an AlGaN/GaN HEMT structure can be functionalized through the chemical modification with anti-*P. marinus* antibody to detect *P. marinus* in the infected waters directly. Due to the natural life cycle of *P. marinus*, the specific antigens were released into waters from *P. marinus* which provide the chance to detect the existence of *P. marinus* in waters. This simple electronic detection of *P. marinus* is the fastest, simplest and cheapest way to detect this bacteria and significantly steps toward a field-deployed sensor chip, which can be integrated with a commercial available wireless transmitter to realize a real-time, fast response and high sensitivity *P. marinus* detector.

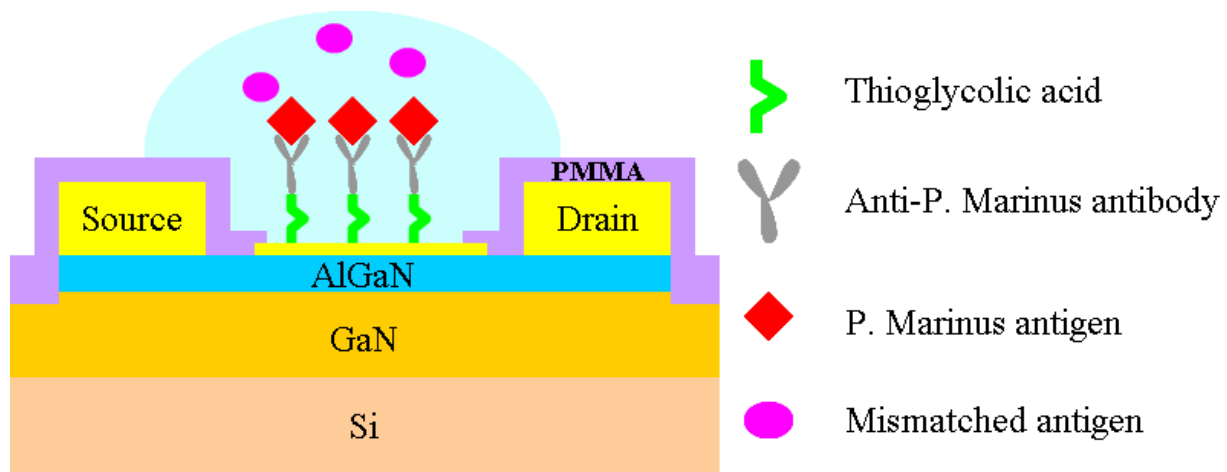
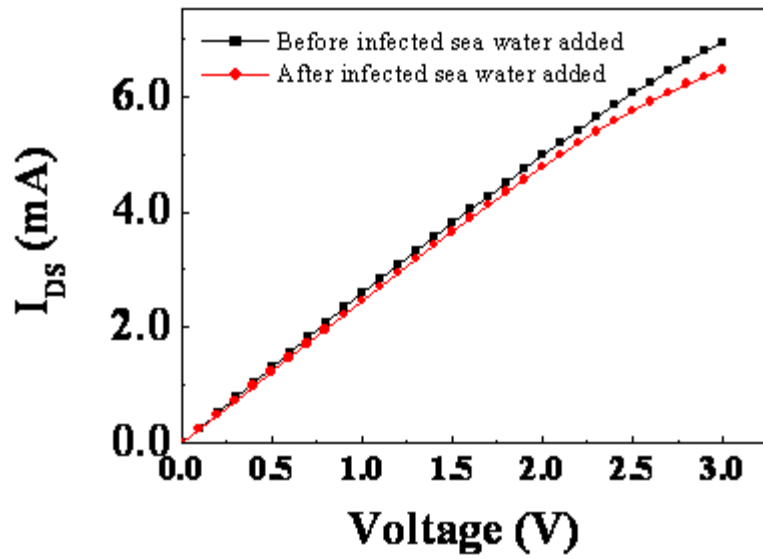
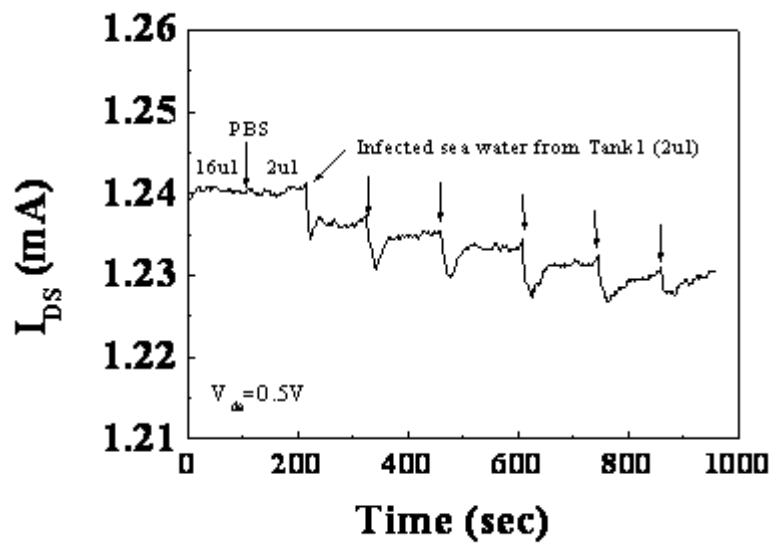


Figure 4-6. Schematic of AlGaN/GaN HEMT sensor. The Au-coated gate area was functionalized with anti-*Perkinsus marinus* antibody/ *Perkinsus marinus* antigen on thioglycolic acid.



A)



B)

Figure 4-7. DC response of the antibody-functionalized AlGaIn/GaN HEMT to *Perkinsus marinus*-infected sea water. A) I-V characteristics of the sensor before and after exposure to the *Perkinsus marinus*-infected sea water from the tank 1. B) Drain current of an AlGaIn/GaN HEMT versus time for *P. marinus* detection in the infected sea water from the tank 1.

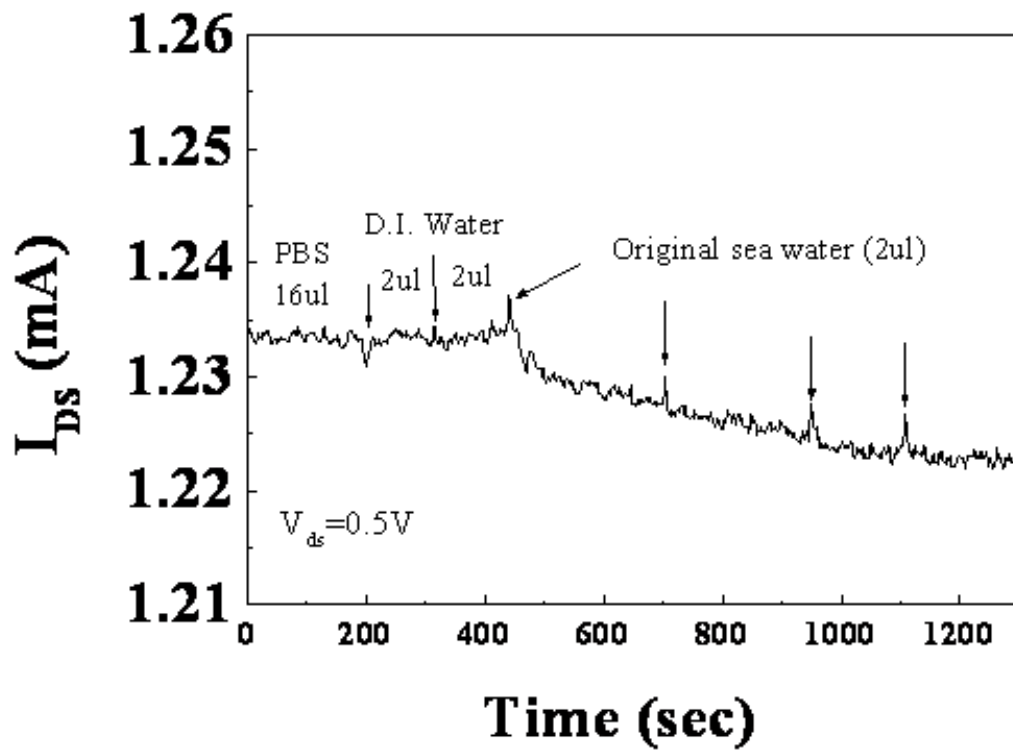
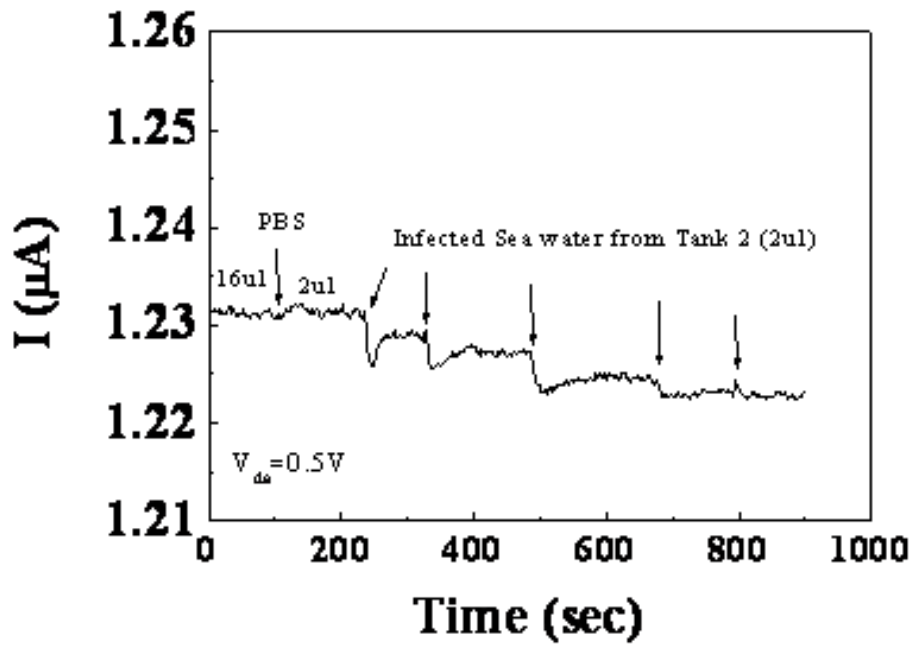
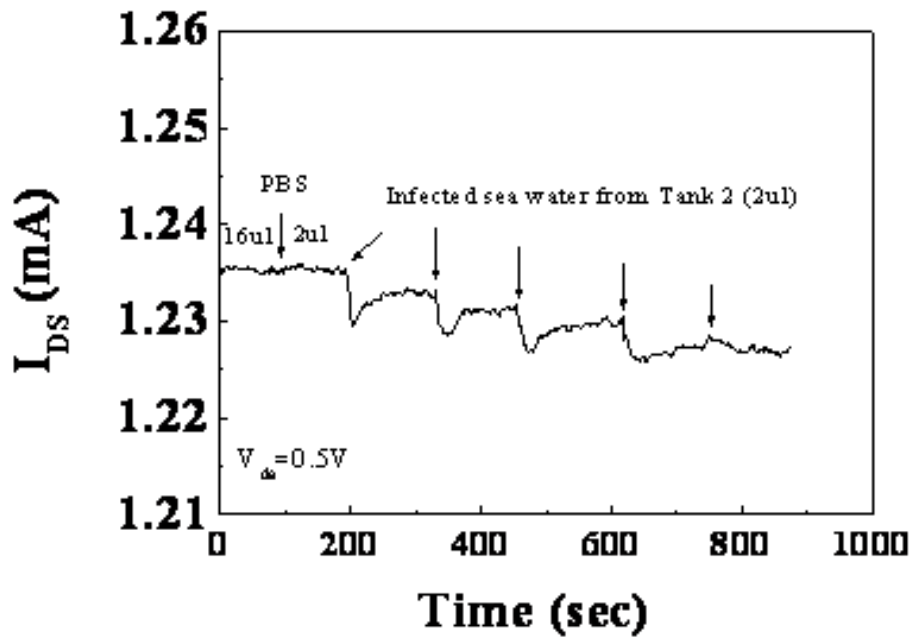


Figure 4-8. Drain current of an AlGaIn/GaN HEMT versus time for *P. marinus* detection in the original sea water.



A)



B)

Figure 4-9. Real-time detection of *P. marinus* in an infected sea water from the tank 2. A) before B) after recycling the sensor with PBS wash.

CHAPTER 5 CONCLUSIONS

5.1 Hydrogen Effects on ZnO Light-emitting Diodes

In this dissertation, hydrogen from different sources would degrade ZnO LEDs on both optical and electrical properties. Hydrogen is a shallow donor, which can increase the conductivity of n-type ZnO films or compensate the p-type dopants in the ZnO films. Hydrogen easily diffused into ZnO films because of its high diffusivity. This high diffusivity can be explained by its small atomic weight and size. Hydrogen concentration can easily reach a concentration of 10^{17}cm^{-3} in ZnO films by exposing the sample in the hydrogen-containing ambient. Due to the nature of difficulty to obtain high hole concentration in p-type ZnO films, hydrogen can convert p-type layer to n-type ZnO and the rectifying characteristics of diodes disappeared. During the processing, the sample was exposed to the solutions and plasma containing plasma and there was no light emission and no rectifying characteristics for the as fabricated LEDs. A thermal annealing at 350°C recovered the diode rectifying characteristics and light emission. The annealed diodes showed band-edge electroluminescence (385nm) and a broad defect band with a peak at 930nm at room temperature. A hydrogen plasma was also used to deliberately introduce hydrogen into the annealed p-i-n ZnO LEDs to verify it's the hydrogen passivation effect on diode characteristics. After the hydrogen plasma treatment, the diode reverse-bias leakage current increased, and both the turn-on voltage and the intensity of the electroluminescence decreased. Moreover, the effects of moisture, water, and phosphoric acid solution on the annealed diode characteristics were also investigated and a significant degradation of electrical and optical properties were observed in all cases. The high diffusivity of hydrogen makes hydrogen easily diffuse into ZnO films, but on the other hand, it makes

hydrogen be easily driven out of the ZnO films with a thermal annealing. Therefore, it is an important to encapsulate ZnO LEDs from the hydrogen passivation effect.

The effectiveness of dielectric encapsulation for the ZnO LEDs was investigated. Plasma-enhanced chemical vapor-deposited SiO₂ and SiN_x was used to encapsulate ZnO heterojunction light emitting diodes. Post-dielectric deposition annealing was found to be very critical for obtaining good LED electrical and optical characteristics. The SiO₂ and SiN_x had very different encapsulate effects in terms of the electrical and electro-luminescence characteristics of the LEDs. Since hydrogen presented during SiO₂ and SiN_x deposition, there was a thermal annealing required to activate the ZnO LEDs after the dielectric deposition. After thermal annealing, the SiO₂ encapsulated ZnO LEDs showed diode IV characteristics and emitted light. However, the annealed SiN_x- encapsulated ZnO LEDs showed leaky diode characteristics and no light emission. We attributed these differences to the role of hydrogen on the LEDs. FTIR spectrum showed rich hydrogen residue in PECVD SiN_x film while no hydrogen residue was found in PECVD SiO₂ after the thermal annealing.

5.2 Indium Zinc Oxide Thin Film Transistors

Enhancement mode and depletion mode indium zinc oxide (IZO) thin film transistors (TFTs) were fabricated on glass substrates using rf magnetron sputtering deposition at room temperature. Plasma enhanced chemical vapor deposited SiO₂ or SiN_x was used as the gate insulator. The enhancement mode TFTs showed excellent pitch-off and the threshold voltage was 0.75V. The drain current on-to-off ratio was $>10^6$. The maximum field effect mobility in the channel was $39.7 \text{ cm}^2 \cdot \text{V}^{-1} \cdot \text{s}^{-1}$. The depletion mode TFTs had a threshold voltage of -2.5V. The drain current on-to-off ratio was $>10^5$. The maximum field effect mobility in the channel was $14.5 \text{ cm}^2 \cdot \text{V}^{-1} \cdot \text{s}^{-1}$. The frequency response are measured at $V_{GS}=0\text{V}$ and $V_{DS}=3\text{V}$. The cut-off

frequency, f_t , is 180MHz and the maximum oscillation frequency, f_{max} , is 155MHz. A T-model was used to extract the device parasitic parameters.

5.3 AlGaIn/GaN High Electron Mobility Transistor-Based Biosensors

Antibody-functionalized Au-gated AlGaIn/GaN high electron mobility transistors (HEMTs) were used for detecting botulinum neurotoxin and *P. marinus* bacteria. The botulinum toxin and the *P. marinus* were specifically recognized through the immobilized antibodies on the gate area. The HEMT based botulinum sensor detected a range of concentrations from 0.1 ng/ml to 100 ng/ml. The change of sensor drain current showed a saturation for the botulinum toxin concentration or above 10ng/ml. The *P. marinus* sensors were used to directly detect the specific protein in the waters where clams were living and dead. Both sensors showed fast response from 5~30 seconds when exposure to the target species. These results demonstrated that the AlGaIn/GaN based biosensors are promising for the applications of fast, highly sensitive, low cost and easy-to-used biosensings.

LIST OF REFERENCES

1. D.C. Look, Mater. Sci. Eng. B **80**, 383 (2001).
2. S.J. Pearton, D.P. Norton, K. Ip, Y.W. Heo, and T. Steiner, Prog. Mater. Sci. **50**, 293 (2005).
3. G-C.Yi, C. Wang and W. I. Park, Semicond. Sci. Technol. **20**, S22 (2005).
4. Ya.I. Alivov, E.V. Kalinina, A.E. Cherenkov, D.C. Look, B.M. Ataev, A.K. Omaev, M.V. Chukichev, and D.M. Bagnall, Appl. Phys. Lett. **83**, 4719 (2003).
5. A. Osinsky, J.W. Dong, M.Z. Kauser, B. Hertog, A.M. Dabiran, P.P. Chow, S.J. Pearton, O. Lopatiuk, and L. Chernyak, Appl. Phys. Lett. **85**, 4272 (2004).
6. S.J. Pearton, D.P. Norton, K. Ip, Y.W. Heo, and T. Steiner, Superlattices and Microstructures **34**, 3 (2003)
7. Y.W. Heo, S.J. Park, K. Ip, S.J. Pearton, and D.P. Norton, Appl. Phys. Lett. **83**, 1128 (2003).
8. S. B. Zhang, S.-H. Wei, and A.Zunger, Phys. Rev. B **63**, 075205 (2001)
9. Y.W. Heo, K. Ip, S.J. Park, S.J. Pearton, and D.P. Norton, Applied Physics A-Materials Science & Processing **78**, 53 (2004)
10. D.C. Look, B. Claflin, Physica Status Solidi B **241**, 624 (2004).
11. Y.J. Li, Y.W. Heo, Y. Kwon, K. Ip, S.J. Pearton, D.P. Norton, Appl. Phys. Lett. **87**, 072101 (2005).
12. Y.W. Heo, Y.W. Kwon, Y. Li, S.J. Pearton, and D.P. Norton, Appl. Phys. Lett. **84**, 3474 (2004).
13. F. A. Selim, M. H. Weber, D. Solodovnikov, Phys. Rev. Lett. **99**, 085502 (2007).
14. C. G. Van de Walle, Phys. Rev. Lett. **85**, 1012 (2000).
15. L. S. Vlasenko and G. D. Watkins, Phys. Rev. B **71**, 125210 (2005).
16. S. Y. Myong and K. S. Lim, Organic Electronics **8**, 51-56 (2007)
17. C. F. Windisch, G. Y. Exarhos, C. H. Yao, J. Appl. Phys. **101**, 123711 (2007)
18. Y. M. Strzhemechny, H. L. Mosbacker, S. H. Goss, J. Electron. Mater. **34**, 399 (2005)
19. E. V. Lavrov, F. Borrnert, J. Weber, Physica B, **376-377**, 694 (2006)

20. D. M. Hofmann, A. Hofstaetter, F. Leiter, H. Zhou, F. Henecker, B. K. Meyer, S. B. Orlinskii, J. Schmidt, P. G. Baranov, *Phys. Rev. Lett.*, **88**, 045504 (2002).
21. G. A. Shi, M. Saboktakin, M. Stavola, and S. J. Pearton, *Appl. Phys. Lett.* **85**, 5601 (2004)
22. K. Ip, M. E. Overberg, Y. W. Heo, D. P. Norton, S. J. Pearton, C. E. Stutz, S. O. Kucheyev, C. Jagadish, J. S. Williams, B. Luod, F. Ren, D. C. Look and J. M. Zavada, *Solid-State Electronics* **47**,12, 2255 (2003).
23. N. H. Nickel and K. Fleischer *Phys. Rev. Lett.* **90**, 197402(2003).
24. C. H. Seager and S. M. Myers , *J. Appl. Phys.* **94**, 2888 (2003).
25. Y. M. Strzhemechny, J. Nemergut, P. E. Smith, J. Bae, D. C. Look, and L. J. Brillson , *J. Appl. Phys.* **94**, 4256 (2003).
26. N. H. Nickel and K. Brendel , *Phys. Rev. B* **68**, 193303 (2003)
27. Y. M. Strzhemechny, H. L. Mosbacker, D. C. Look, D. C. Reynolds, C. W. Litton, N. Y. Garces, N. C. Giles, L. E. Halliburton, S. Niki, and L. J. Brillson *Appl. Phys. Lett.* **84**, 2545 (2004).
28. L. E. Halliburton, Lijun Wang, Lihua Bai, N. Y. Garces, N. C. Giles, M. J. Callahan, and B. Wang , *J. Appl. Phys.* **96**, 7168 (2004).
29. E. V. Lavrov, F. Börrnert, and J. Weber, *Phys. Rev. B* **71**, 035205 (2005).
30. C. A. Wolden, T. M. Barnes, J. B. Baxter, and E. S. Aydil , *J. Appl. Phys.* **97**, 043522 (2005).
31. X. Li, B. Keyes, S. Asher, S. B. Zhang, Su-H. Wei, T. J. Coutts, S. Limpijumnong and C. G. Van de Walle, *Appl. Phys. Lett.* **86**, 122107 (2005).
32. S. Limpijumnong and S. B. Zhang, *Appl. Phys. Lett.* **86**, 151910 (2005) .
33. E. V. Lavrov, F. Börrnert and J. Weber , *Phys. Rev. B* **72**, 085212 (2005) .
34. S. J. Jokela and M. D. McCluskey, *Phys. Rev. B* **72**, 113201 (2005).
35. E. V. Monakhov, J. S. Christensen, K. Maknys, B. G. Svensson and A. Yu. Kuznetsov, *Appl. Phys. Lett.* **87**, 191910 (2005).
36. G. A. Shi, M. Stavola, S. J. Pearton, M. Thieme, E. V. Lavrov and J. Weber, *Phys. Rev. B* **72**, 195211 (2005).
37. E. V. Lavrov and J. Weber , *Phys. Rev. B* **73**, 035208 (2006).
38. K. J. Allen, *Proceed. IEEE.* **93**, 1394, (2005).

39. K. Jain, M. Klosner, M. Zemel, S. Raghunandan, *Proceed. IEEE.* **93**, 1500, (2005).
40. Y. Sun and J. A. Rogers, *Adv. Mater.* **19**, 1897 (2007).
41. D. Y. Ku, I. H. Kim, I. Lee, K. S. Lee, T. S. Lee, J. -h. Jeong, B. Cheong, Y. -J. Baik, W. M. Kim, **515**, 1364 (2006).
42. H. C. Pan, M. H. Shiao, C. Y. Su, and C. N. Hsiao, *J. Vac. Sci. Technol. A* **23**, 1187 (2005).
43. H. Yabuta, M. Sano, K. Abe, T. Aiba, T. Den, H. Kumomi, K. Nomura, T. Kamiya, and H. Hosono, *Appl. Phys. Lett.* **89**, 112123 (2006).
44. T. Minami, *J. Vac. Sci. Technol. A* **17**, 1765 (1999).
45. T. Sasabayashi, N. Ito, E. Nishimura, M. Kon, P. K. Song, K. Utsumi, A. Kaijo, and Y. Shigesato, *Thin Solid Films*, **445**, 219 (2003).
46. S.S. Arnon , R. Schechter and T.V.Inglesby T. V. *JAMA*, **285**, No. 8, 256 (2001).
47. R.A. Greenfield , B.R. Brown , J.B. Hutchins J.J. Iandolo , R. Jackson, L.N. LSlater, and M.S. Bronze, *The American J. Of The Medical Sciences*, **323**, 326 (2002).
48. J. S. Michaelson, E. Halpern and D.B. Kopans, *Radiology* **212(2)**. 551 (1999).
49. T. Harrison, L.Bigler, M.Tucci, L.Pratt, F. Malamud, J.T. Thigpen, C. Streckfus and H. Younger, *Spec. Care Dentist* **18(3)**, 109 (1998) .
50. R. McIntyre, L. Bigler, T. Dellinger, M. Pfeifer, T. Mannery and C. Streckfus, *Oral Surg Oral Med. Oral Pathol. Oral Radiol. Endod.* **88(6)**, 687 (1999).
51. C. Streckfus, L. Bigelr, T. Dellinger, M. Pfeifer, A. Rose and J.T. Thigpen, *Clin. Oral Investig.* **3(3)**, 138 (1999).
52. C. Streckfus, L. Bigler, T. Dellinger, X.Dai, A. Kingman and J.T. Thigpen, *Clin Cancer Res.* **6(6)**, 2363 (2000).
53. C. Streckfus, L. Bigler, M. Tucci and J.T. Thigpen, *Cancer Invest* **18(2)**, 101 (2000).
54. C. Streckfus, L. Bigler, T. Dellinger, X. Dai, W.J. Cox, A. McArthur, A. Kingman and J.T. Thigpen, *Oral Surg Oral Med Oral Pathol. Oral Radiol. Endod.* **91(2)**, 174 (2001).
55. L. R. Bigler, C.F. Streckfus, L. Copeland, R. Burns, X. Dai, M. Kuhn, P. Martin and S. Bigler, *J Oral Pathol. Med* **31(7)**, 421 (2002).
56. C. Streckfus and L. Bigler, *Adv. Dent. Res* **18(1)**, 17 (2005).
57. C. F. Streckfus, L. R. Bigler and M. Zwick, *J Oral Pathol. Med* **35(5)**, 292(2006).

58. W.R. Chase, J Mich. Dent. Assoc. **82(2)**, 12(2000).
59. S.Z. Paige and C.F. Streckfus, Gen Dent **55(2)**, 156(2007).
60. M.A. Navarro, R. Mesia, O. Diez-Giber, A. Rueda, B. Ojeda and M.C. Alonso, Breast Cancer Res. Trea. **42(1)**, 83(1997).
61. K.Bagramyan, J.R. Barash, S.S. Arnon and M. Kalkum M, Matrices PLoS ONE **3**, 2041(2008).
62. A. P. Zhang, L. B. Rowland, E. B. Kaminsky, V. Tilak, J. C. Grande, J. Teetsov, A. Vertiatchikh and L. F. Eastman, J.Electron.Mater.**32**, 388(2003).
63. O. Ambacher, M. Eickhoff, G. Steinhoff, M. Hermann, L. Gorgens, V. Werss, B. Baur, M. Stutzmann, R. Neuterger, J. Schalwig, G. Muller, V. Tilak, B. Green, B. Schafft, L. F. Eastman, F. Bernadini, and V. Fiorienbini, Proc. ECS **02-14**, 27 (2002).
64. R. Neuberger, G. Muller, O. Ambacher and M. Stutzmann, Phys. Stat. Soli. A **185**, 85 (2001).
65. J. Schalwig, G. Muller, O. Ambacher and M. Stutzmann, Phys. Stat. Solidi A **185**, 39 (2001).
66. G. Steinhoff, M. Hermann, W. J. Schaff, L. F. Eastman, M. Stutzmann and M. Eickhoff, Appl. Phys. Lett. **83**, 177 (2003).
67. M. Eickhoff, R. Neuberger, G. Steinhoff, O. Ambacher, G. Muller, and M. Stutzmann, Phys. Stat. Solidi B **228**, 519 (2001).
68. B.S. Kang, H.T. Wang, F. Ren and S.J.Pearton, J.Apl.Phys.**104**, 031101 (2008).
69. B. S. Kang, S. Kim, F. Ren, J. W. Johnson, R. Therrien, P. Rajagopal, J. Roberts, E. Piner, K. J. Linthicum, S. N .G. Chu, K. Baik, B. P. Gila, C. R. Abernathy and S. J. Pearton, Appl. Phys.Lett. **85**, 2962 (2004).
70. S. J. Pearton, B. S. Kang, S. Kim, F. Ren, B. P.Gila, C. R. Abernathy, J. Lin and S. N. G. Chu, J. Phys: Condensed Matter. **16** R961 (2004).
71. G. Steinoff, O. Purrucker, M. Tanaka, M. Stutzmann and M. Eickoff, Adv. Funct. Mater. **13**, 841 (2003).
72. G. Steinhoff, B. Baur, G. Wrobel, S. Ingebrandt, A. Offenhauser, A. Dadgar, A. Krost, M.Stutzmann and M.Eickhoff, Appl. Phys. Lett. **86**, 033901 (2005).
73. B. S. Kang, H. T. Wang, F. Ren, S. J. Pearton, T. E. Morey, D. M. Dennis, J. W. Johnson, P. Rajagopal, J. C. Roberts, E. L. Piner, and K. J. Linthicum, Appl. Phys. Lett. **91**, 252103 (2007).

74. B. S. Kang, F. Ren, L. Wang, C. Lofton, Weihong Tan, S. J. Pearton, A. Dabiran, A. Osinsky, and P. P. Chow, *Appl. Phys. Lett.* **87**, 023508 (2005).
75. B. S. Kang, J.J. Chen, F. Ren, S. J. Pearton, J.W. Johnson, P. Rajagopal, J.C. Roberts, E.L. Piner, and K.J. Linthicum, *Appl. Phys. Lett.* **89**, 122102 (2006).
76. J. D. Andrews, *American Fisheries Society Special Publication* **18**, 47 (1998).
77. E.M. Bureson, and L. M. Ragone-Calvo, *J. Shellfish Research* **15**, 17 (1996).
78. S. E. Ford, *J. Shellfish Research* **15**, 45 (1996).
79. A. Villalba, K. S. Reece, M. C. Ordás, S. M. Casas, A. Figueras, *Aquatic Living Resources* **17**, 411 (2004).
80. W. T. Pecher, M. R. Alavi, E. J. Schott, J. A. Fernandez-Robledo, L. Roth, S. T. Berg, G. R. Vasta, *J. Parasitol.* **94**(2), 410 (2008).
81. S. M. Ray, *Proc. Natl. shellfish. Assn.* **54**, 55 (1966).
82. K. S. Reece, C. F. Dungan, 2006. *Perkinsus* sp. infections of marine molluscs. *In: AFS-FHS blue book: 2005 edition, Chapter 5.2.1-17 Fish Health Section, American Fisheries Society, Bethesda, Maryland.*
83. S. F. J. Cox, E. A. Davis, S. P. Cottrell, P. J. C. King, J. S. Lord, J. M. Gil, H. V. Alberto, R. C. Vilão, J. Piroto Duarte, N. Ayres de Campos, A. Weidinger, R. L. Lichti, and S. J. C. Irvine, *Phys. Rev. Lett.* **86**, 2601 (2001)
84. M. S. Oh, D. K. Hwang, J. H. Lim, Y. S. Choi, and S. J. Park, *Appl. Phys. Lett.* **91**, 212102 (2007).
85. Y. L. Wang, F. Ren, H. S. Kim, S. J. Pearton, and D. P. Norton, *Appl. Phys. Lett.* **90**, 092116 (2007)
86. K. Ip, M.E. Overberg, Y.W. Heo, D.P. Norton, S.J. Pearton, C.E. Stutz, B. Luo, F. Ren, D.C. Look, and J.M. Zavada, *Appl. Phys. Lett.* **82**, 385 (2003).
87. K. Ip, M.E. Overberg, Y.W. Heo, D.P. Norton, S.J. Pearton, S.O. Kucheyev, C. Jagadish, J.S. Williams, R.G. Wilson, J.M. Zavada, *Appl. Phys. Lett.* **81**, 3996 (2002).
88. M. Hong, M. Passlack, J. P. Mannaerts, J. Kwo, S. N. G. Chu, N. Moriya, S. Y. Hou, and V. J. Fratello, *J. Vac. Sci. Technol. B* **14**, 2297 (1996).
89. O. Schmidt, A. Geis, P. Kiesel, C. G. Van de Walle, N. M. Johnson, A. Bakin, A. Waag, G. H. Döhler, *Superlatt. Microstr.* **39**, 8 (2006).
90. H. S. Kim, S. J. Pearton, D. P. Norton, F. Ren, *J. Appl. Phys.* **102**, 104904 (2007).

91. T. Minami, S. Takata, M. Yamanishi and T. Kawamura, *Jpn. J. Appl. Phys.* **18**, 1617 (1979).
92. K.-K. Kim, H.S. Kim, D.-K. Hwang, J.-H. Lim, and S.-J. Park, *Appl. Phys. Lett* **83**, 63 (2003).
93. Y. L. Wang, H. S. Kim, D. P. Norton, S. J. Pearton, and F. Ren, *Electrochem. Solid-State Lett.* **11**, 88 (2008).
94. A. K. Kullarni, K. H. Schula, T. S. Lim, and M. Khan, *Thin Solid Films* **308**, 1, (1997).
95. K. Zhang, F. Zhu, C. H. A. Huan, and A. T. S. Wee, *Thin Solid Films* **376**, 255, (2000).
96. H. Kim, C. M. Gilmore, A. Piqué, J. S. Horwitz, H. Mattoussi, H. Murata, Z. H. Kafafi, and D. B. Chrisey, *J. Appl. Phys.* **86**, 6451 (1999).
97. K. Nomura, H. Ohta, A. Takagi, T. Kamiya, M. Hirano and H. Hosono, *Nature* **432**, 288 (2004).
98. E. Fortunato, P. Barquinha, A. Pimentel, A. Gonçalves, A. Marques, R. Martins and L. Pereira, *Appl. Phys. Lett.*, **85**, 2541 (2004).
99. N. L. Dehuff, E. S. Kettenring, D. Hong, H. Q. Chiang, J. F. Wager, R. L. Hoffman, C.-H. Park and D. A. Keszler, *J. Appl. Phys.* **97**, 064505 (2005).
100. E. Fortunato, P.M.C. Barquinha, A.C.M.B.G. Pimentel, A.M.F. Gonçalves, A.J.S. Marques, L.M.N. Pereira and R. Martins, *Adv. Mater.*, **17**, 590 (2005).
101. J. Cui, A. Wang, N.L. Edleman, J. Ni, P. Lee, N.R. Armstrong and T.J. Marks, *Adv. Mater.* **31**, 1476 (2001).
102. G. Hu, B. Kumar, H. Gong, E.F. Chor and P. Wu, *Appl. Phys. Lett.* **88**, 101901 (2006).
103. A. Wang, J. Dai, J. Cheng, M.P. Chudzik, T.J. Marks, R.P.H. Chang and C.R. Kannewurf, *Appl. Phys. Lett.* **73**, 327 (1998).
104. K. Tominaga, T. Takao, A. Fukushima, T. Moriga and I. Nakabayashi, *Vacuum* **66**, 505 (2002).
105. N. Naghavi, C. Marcel, L. Dupont, A. Rougier, J.B. Leriche and C. Guery, *J. Mater. Chem.* **10**, 2315 (2000).
106. S.Y. Lee and B.O. Park, *Thin Solid Films* **484**, 184 (2005).
107. J. Park, J. Song, Y.W. Heo, J.H. Lee, J.J. Kim, W.T. Lim, L. Stafford, D.P. Norton and S.J. Pearton, *J. Vac. Sci. Technol. B* **24**, 2737 (2006).
108. E. M. C. Fortunato, P. M. C. Barquinha, A. C. M. B. G. Pimentel, A. M. F. Gonçalves, A. J. S. Marques, L. M. N. Pereira and R. F. P. Martins, *Adv. Mater.* **17**, 590 (2005).

109. Y. Kwon, Y. Li, Y. W. Heo, M. Jones, P. H. Holloway, D. P. Norton, Z.V. Park and S. Li, *Appl. Phys. Lett.* **84**, 2685 (2004).
110. Y. W. Heo, B.S. Kang, L.C. Tien, Y. Kwon, D.P. Norton, F. Ren and S.J. Pearton, *Appl. Phys. Lett.* **85**, 2274 (2004).
111. H.-H. Hsieh and C.-C. Wu, *Appl. Phys. Lett.* **89**, 041109 (2006).
112. J. Siddiqui, E. Cagin, D. Chen and J. D. Phillips , *Appl. Phys. Lett.* **88**, 212903 (2006).
113. P. F. Garcia, R. S. McLean, and M. H. Reilly, *Appl. Phys. Lett.* **88**, 123509 (2006).
114. S. Sasa, M. Ozaki, K. Koike, M. Yano and M. Inoue, *Appl. Phys. Lett.* **89**, 053502 (2006).
115. H. Q. Chiang and J. F. Wager, R. L. Hoffman, J. Jeong and D. A. Keszler, *Appl. Phys. Lett.* **86**, 013503 (2005).
116. N. Ito, Y. Sato, P.K. Song, A. Kaijio, K. Inoue and Y. Shigesato, *Thin Solid Films* **496**, 99 (2006).
117. Yeon Sik Jung, Ji Yoon Seo, Dong Wook Lee and Duk Young Jeon, *Thin Solid Films* **445**, 63 (2003).
118. P. F. Carcia, R. S. McLean, and M. H. Reilly, and G. Nunes, *Appl. Phys. Lett.* **82**, 1117 (2003).
119. E. Fortunato, A. Pimentel, L. Pereira ,A. Gonçalves, G. Lavareda, H. Aguas, I. Ferreira, C. N. Carvalho, and R. Martins, *J. Non-Cryst. Solids*, **338-340**, 806 (2004).
120. R. E. Presley, C. L. Munsee, C. -H. Park, D. Hong, J. F. Wager, and D. A. Keszler, *J. Phys. D.* **37**, 2810 (2004).
121. Dhananjay, C. W. Chu, *Appl. Phys. Lett.*, **91**, 132111 (2007).
122. H. Hosono, *J. Non-Cryst. Solids*, **352**, 851 (2006).
123. M. Orita, H. Ohta, M. Hirano, S. Narushima, H. Hosono, *Phil. Mag. B*, **81**,501 (2001).
124. Yu-Lin Wang, F. Ren, Wantae Lim, D.P. Norton, S.J.Pearton, I.I. Kravchenko, J.M.Zavada, *Appl. Phys. Lett.*, **90**, 1 (2007)
125. R. Martins, P. Barquinha, I. Ferreira, L. Pereira, G. Goncalves, and E. Fortunato, *J. Appl. Phys.* **101**, 044505 (2007).
126. H. Hosono, Y. Yamashita, N. Ueda, and H. Kawazoe, *Appl. Phys. Lett.* **68**,29 (1996).
127. M. Yasukawa, H. Hosono, N. Ueda, and H. Kawazoe, *Jpn. J. Appl. Phys. Part 2*, **34**, L281

128. S. Narushima, H. Hosono, J. Jisun, T. Yoko, K. Shimakawa, *J. Non-Cryst. Solids*, **374**, 313 (2000).
129. H. Nakazawa, Y. Ito, E. Matsumoto, K. Adachi, N. Aoki, and Y. Ochiai, *J. Appl. Phys.*, **100**, 093706 (2006)
130. W. Lim, Y. L. Wang, F. Ren, D. P. Norton, I. I. Kravchenko, J. M. Zavada, S. J. Pearton, *Electrochemical and Solid-State Lett.*, **10**, H267 (2007).
131. H. Fujikawa, K. Noda, S. Tokito and Y. Taga, *Appl. Phys. Lett.* **70**, 270 (1997).
132. L. Davis, *Thin Solid Films*, **236**,1 (1993).
133. F. Benkhelifa, P. V. Ashrit, G. Bader, Fernand, E. Girouard, and V. Truong, *Thin Solid Films*, **232**, 83 (1993).
134. B. Kumar and H. Gong, *J. Appl. Phys.*, **98**, 073703 (2005).
135. T. Minami, *MRS Bull.*, **25**,38 (2000).
136. J. M. Philips, et. al., *Appl. Phys. Lett.*, **67**, 2246 (1995)
137. J.-L. Brousseau, H. Bourque, A. Tessier, and R. M. Leblanc, *Appl. Surf. Sci.*, **108**, 351 (1997).
138. A. E. Rakhshani, Y. Makdisi, and H. A. Ramazaniyan, *J. Appl. Phys.*, **83**, 15 (1998).
139. H. Morikawa, and M. Fujita, *Thin Solid Films*, **359**, 61 (2000).
140. E. Terzini, G. Nobile, S. Loreti, C. Minarini, T. Polichetti, P. Thilakan, *Jpn. J. Appl. Phys. Part 1*, **38**, 3448 (1999).
141. B. T. Lee, T. H. Kim, S. H. Jeong, *J. Phys. D. : Appl. Phys.*, **39**, 957 (2006).
142. H. Q. Chiang, D. Hong, C. M. Hung, R. E. Presley, J. F. Wager, C.-H Park, D. A. Keszler and G. S. Herman, *J. Vac.Sci.Tech.* **24**, 2702 (2006).
143. Yu-Lin Wang, F. Ren, Wantae Lim, D.P. Norton, S.J.Pearton, I.I. Kravchenko, J.M.Zavada, *Appl. Phys. Lett.*, **90**, 232103 (2007)

BIOGRAPHICAL SKETCH

Yu-Lin Wang received his B.S. degree in chemistry at Tung-Hai University in 1993 and M.S. degree at National Taiwan University in 1995, respectively, in Taiwan. From 1995 to 1997, he served as first lieutenant in Air Force in Taiwan. After military service, he worked in the semiconductor industry in the research department. He had developed Si and III-V semiconductor-based electronic and photonic devices such as LOGIC, DRAM, LED, HBT..etc. until 2006.

In 2006 fall, he enrolled in the Ph. D. program in the Department of Materials Science and Engineering at University of Florida. He joined Dr. Fan Ren's research group and focused on the wide bandgap semiconductor materials and devices. He worked on ZnO light-emitting diodes, oxide-based thin-film transistors and AlGaIn/GaN high electron mobility transistor-based biosensor. He earned his Doctor of Philosophy degree in materials science and engineering in May 2009. He had 5 oral presentations in international conferences. He is an author or coauthor of more than 30 papers published in referred journals.